











## ORIGINAL ARTICLE

# The temporal evolution of subduction initiation in the Samail ophiolite: High-precision U–Pb zircon petrochronology of the metamorphic sole

Matthew Rioux<sup>1,2</sup>  | Joshua M. Garber<sup>3</sup>  | Michael Searle<sup>4</sup>  |  
James L. Crowley<sup>5</sup>  | Sally Stevens<sup>6</sup>  | Mark Schmitz<sup>5</sup>  |  
Andrew Kylander-Clark<sup>1</sup>  | Kayla Leal<sup>1</sup>  | Tyler Ambrose<sup>4,7</sup>  | Andrew J. Smye<sup>3</sup> 

<sup>1</sup>Department of Earth Science, University of California, Santa Barbara, California, 93106, USA

<sup>2</sup>Earth Research Institute, University of California, Santa Barbara, California, 93106, USA

<sup>3</sup>Department of Geosciences, Pennsylvania State University, University Park, Pennsylvania, 16802, USA

<sup>4</sup>Department of Earth Sciences, University of Oxford, Oxford, OX1 3AN, UK

<sup>5</sup>Department of Geosciences, Boise State University, Boise, Idaho, 83725, USA

<sup>6</sup>Department of Geoscience, University of Wisconsin-Madison, Madison, Wisconsin, 53711, USA

<sup>7</sup>Yukon Geological Survey, Whitehorse, Yukon, Y1A 2C6, Canada

## Correspondence

Matthew Rioux, Department of Earth Science, University of California, Santa Barbara, California 93106, USA.

Email: [mrioux@ucsb.edu](mailto:mrioux@ucsb.edu)

Handling Editor: Prof. Johann Diener

## Funding information

United States National Science Foundation, Grant/Award Numbers: EAR-1650407, EAR-1250522, EAR-2120931

## Abstract

High-precision dating of the metamorphic sole of ophiolites can provide insight into the tectonic evolution of ophiolites and subduction zone processes. To understand subduction initiation beneath a young, well-preserved and well-characterized ophiolite, we performed coupled zircon laser-ablation inductively coupled mass spectrometry trace element analyses and high-precision isotope dilution-thermal ionization mass spectrometry U–Pb dating on 25 samples from the metamorphic sole of the Samail ophiolite (Oman–United Arab Emirates). Zircon grains from amphibolite- to granulite-facies (0.8–1.3 GPa, ~700–900°C), garnet- and clinopyroxene-bearing amphibolite samples ( $n = 18$ ) show systematic trends of decreasing heavy rare earth element slope (HREE; Yb/Dy) with decreasing Yb concentration, reflecting progressive depletion of the HREE during prograde garnet growth. For half of the garnet-clinopyroxene amphibolite samples, Ti-in-zircon temperatures increase, and U–Pb dates young with decreasing HREE slope, consistent with coupled zircon and garnet growth during prograde metamorphism. In the remaining samples, there is no apparent variation in Ti-in-zircon temperature with decreasing HREE slope, and the combined U–Pb and geochemical data suggest zircon crystallization along either the prograde to peak or prograde to initial retrograde portions of the metamorphic  $P$ – $T$ – $t$  path. The new data bracket the timing of prograde garnet and zircon growth in the highest grade rocks of the metamorphic sole between  $96.698 \pm 0.094$  and  $95.161 \pm 0.064$  Ma, in contrast with previously published geochronology suggesting prograde metamorphism at ~104 Ma. Garnet-free amphibolites and leucocratic pods from lower grade (but still upper amphibolite facies) portions of the sole are uniformly HREE enriched (Yb/Dy > 5) and are ~0.5–1.3 Myr younger than the higher grade rocks from the same localities, constraining the temporal offset between the

This is an open access article under the terms of the [Creative Commons Attribution-NonCommercial-NoDerivs](https://creativecommons.org/licenses/by-nc-nd/4.0/) License, which permits use and distribution in any medium, provided the original work is properly cited, the use is non-commercial and no modifications or adaptations are made.

© 2023 The Authors. *Journal of Metamorphic Geology* published by John Wiley & Sons Ltd.

metamorphism and juxtaposition of the higher and lower grade units. Positive zircon  $\varepsilon_{\text{Hf}}$  (+6.5 to +14.6) for all but one of the dated amphibolites are consistent with an oceanic basalt protolith for the sole. Our new data indicate that prograde sole metamorphism (96.7–95.2 Ma) immediately predated and overlapped growth of the overlying ophiolite crust (96.1–95.2 Ma). The ~600 ky offset between the onset of sole metamorphism in the northern portion of the ophiolite versus the start of ophiolite magmatism is an order of magnitude shorter than previously proposed (~8 Ma) and is consistent with either spontaneous subduction initiation or an abbreviated period of initial thrusting during induced subduction initiation. Taken together, the sole and ophiolite crust preserve a record of the first ~1.5 Myr of subduction. A gradient in the initiation of high-grade metamorphism from the northwest (96.7 Ma) to southeast (96.0–95.7 Ma) may record propagation of the nascent subduction zone and/or variations in subduction rate along the length of the ophiolite.

#### KEYWORDS

geochronology, ophiolite, petrochronology, Samail, zircon

## 1 | INTRODUCTION

As the largest and most studied ophiolite in the world, the Samail ophiolite (Oman-United Arab Emirates) has played a key role in our current understanding of ocean ridge processes and the structure of the oceanic crust (e.g., Boudier et al., 1996; Kelemen et al., 1997; Nicolas et al., 1988; Phipps Morgan & Chen, 1993; Quick & Denlinger, 1993). However, several lines of evidence suggest that the Samail ophiolite formed in a supra-subduction zone setting, likely during subduction initiation (Section 2.1) and as a result is also a valuable analogue for studying nascent subduction-zone processes. The ophiolite is underlain by a 'metamorphic sole' (Figure 1), which is interpreted as the initial suite of rocks thrust below the ophiolite (Bailey, 1981; Gass et al., 1983; Nicolas et al., 2000; Searle & Cox, 2002). Elevated pressures ( $\geq 1$  GPa) within the highest grade amphibolites of the metamorphic sole exceed the lithostatic pressures implied by the ~10–15 km thick ophiolite and are consistent with their formation in a nascent subducted slab (Ambrose et al., 2021; Cowan et al., 2014; Gnos, 1998; Hacker & Gnos, 1997; Soret et al., 2017). As such, the Samail metamorphic sole has the potential to provide unique insight into the tectonic development of the ophiolite, including the role of subduction initiation during ophiolite formation.

High-precision geochronology is crucial for determining rates of subduction initiation processes and can provide unique insights into the tectonic mechanisms of initiation. In our previous work, we used the relative timing between sole metamorphism and formation of the

ophiolite crust to support a supra-subduction-zone origin for the Samail ophiolite (Rioux et al., 2016). Building on this work, Guilmette et al. (2018) highlighted how the offset between the timing of sole metamorphism and ophiolite magmatism can be used to differentiate between existing models for subduction initiation (induced versus spontaneous; Stern, 2004). In this framework, during *induced* subduction initiation, initial development of subduction is triggered by regional compression prior to the onset of subduction, and as a result, metamorphism in the sole related to early thrusting may predate ophiolite formation by several million years (e.g., Gurnis et al., 2004; Leng et al., 2012). In contrast, in *spontaneous* subduction initiation, density differences between two adjacent pieces of oceanic crust lead to spontaneous sinking of a plate into the mantle, and sole metamorphism is predicted to be (nearly) synchronous with ophiolite magmatism (e.g., Maunder et al., 2020; Stern & Bloomer, 1992). Both of these processes have been numerically modelled (e.g., Gerya, 2011; Gerya et al., 2008; Gurnis et al., 2004; Hall et al., 2003; Leng et al., 2012; Maunder et al., 2020; Nikolaeva et al., 2008), but the relative importance of each process on Earth, and whether model timescales match those of natural processes, is still poorly constrained (Guilmette et al., 2018; Stern, 2004; Stern & Gerya, 2018; Zhou & Wada, 2021).

While the importance of precise geochronology for understanding subduction initiation processes and the tectonic development of the Samail ophiolite is clear, the timing and duration of sole metamorphism is currently debated. In our previous work, we found that high-

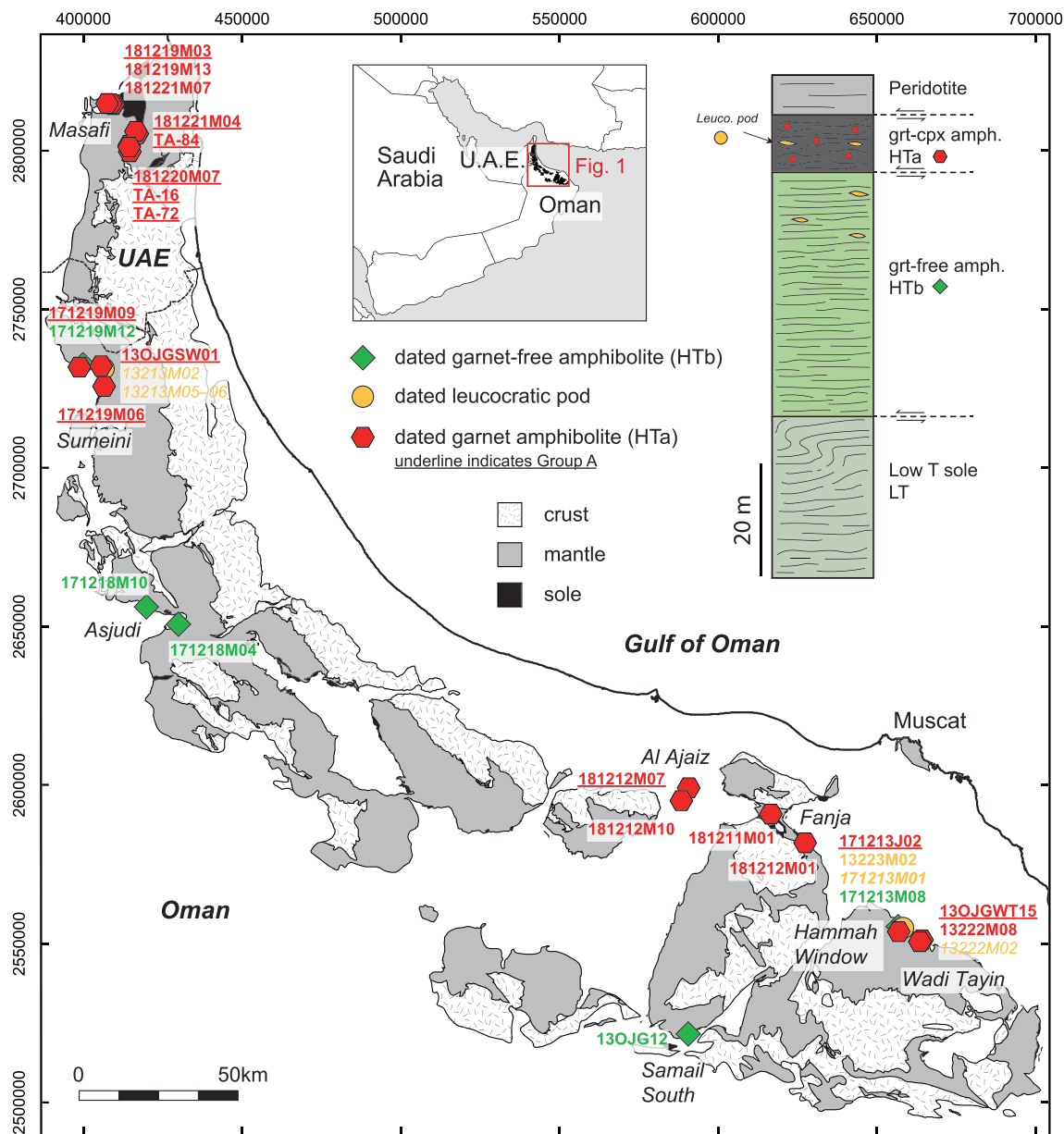


**FIGURE 1** Geologic map of the Samail (Oman-United Arab Emirates) ophiolite. Inset shows the location map and a simplified stratigraphy for the metamorphic sole (after Soret et al., 2017). Sample locations from the metamorphic sole from this study (bold) and Rioux et al. (2016, italic) are plotted. Sole locality names are in italics. Map after Nicolas et al. (2000)

precision U–Pb zircon dates from leucocratic pods and a garnet amphibolite within the Samail metamorphic sole record metamorphism from ~96.2–94.8 Ma (Rioux et al., 2016), overlapping or slightly predating the formation of the ophiolite crust (96.1–95.2 Ma) (Rioux et al., 2012, 2013, 2016; Rioux, Garber, et al., 2021). These data are consistent with earlier K–Ar and  $^{40}\text{Ar}/^{39}\text{Ar}$  studies of the sole, which suggested sole metamorphism either overlapped or directly post-dated ophiolite formation (Gnos & Peters, 1993; Hacker et al., 1996; Montigny et al., 1988). In contrast, Guilmette et al. (2018) reported

garnet-whole rock Lu–Hf isochron dates of ~104–103 Ma from the same sole localities. These authors interpreted the Lu–Hf dates to record prograde garnet growth, and the zircon U–Pb dates to record zircon crystallization from amphibolite melts during retrograde cooling, requiring that the sole remained at supra-solidus temperatures for ~8 Myr. The ~8 Ma offset between the older Lu–Hf dates and the timing of ophiolite magmatism was taken as evidence for induced subduction initiation.

The disparate dates from the metamorphic sole currently limit meaningful interpretation of the offset

between sole and ophiolite formation, and thus the tectonic conditions of sole development. To better constrain the temporal evolution of the metamorphic sole of the Samail ophiolite, we present new high-precision U–Pb zircon dates from 25 samples from the sole along the length of the ophiolite. Coupled zircon U–Pb and trace element data directly link the high-precision dates to metamorphic processes—including garnet growth—providing new insight into the timing of prograde metamorphism in the Samail ophiolite, variations in the timing of sole metamorphism along the length of the ophiolite and the relative timing of metamorphism in different units within the sole. New zircon Hf isotopic data place constraints on the composition of the sole protolith.

## 2 | GEOLOGIC BACKGROUND

### 2.1 | The tectonic setting of ophiolite formation

The Samail Ophiolite is the largest, best-preserved and best-exposed ophiolite in the world. Decades of research on the ophiolite have shown that it is a thrust slice of Cretaceous-aged fast-spread oceanic crust and upper mantle (Gass et al., 1983; Hopson et al., 1981; MacLeod & Rothery, 1992; Nicolas, 1989; Nicolas et al., 1996; Pallister & Hopson, 1981; Rioux et al., 2012; Searle & Cox, 1999; Tilton et al., 1981; Warren et al., 2005) that formed during the approach and collision of the Arabian plate with Eurasia (Agard et al., 2007). The tectonic setting of the Samail ophiolite has long been controversial, with endmember models envisioning formation at a normal mid-ocean ridge spreading centre (Boudier et al., 1988; Nicolas & Boudier, 2017) or in a supra-subduction zone setting (Alabaster et al., 1982; Pearce et al., 1981; Searle & Cox, 1999; Searle & Malpas, 1980, 1982). However, several lines of evidence, including numerous recent studies, strongly favour a supra-subduction zone origin:

1. Geochemical data show that both early (V1) and late (V2) ophiolite lavas were likely hydrous and that even lavas within the early V1 series have geochemical signatures suggesting a subduction component (Alabaster et al., 1982; Belgrano & Diamond, 2019; Ernewein et al., 1988; MacLeod et al., 2013; Pearce et al., 1981).
2. High peak metamorphic pressures (0.8–1.3 GPa) for the highest grade sole rocks suggest that they were metamorphosed in a subducting slab below the ophiolite (Ambrose et al., 2021; Cowan et al., 2014; Gnos, 1998; Hacker & Gnos, 1997; Searle & Cox, 2002).
3. Geochemical evidence suggests that the protolith of the metamorphic sole had a different composition than the ophiolite lavas, arguing against emplacement of the ophiolite over adjacent oceanic crust of the same composition, as would be expected if thrusting initiated along a mid-ocean ridge (Searle & Malpas, 1982).
4. High-precision U–Pb zircon dating indicates that sole metamorphism (96.2–94.8 Ma) was synchronous with or immediately predated formation of the ophiolite crust (96.1–95.2 Ma), requiring the presence of a subducted slab at the time of ophiolite formation (Guilmette et al., 2018; Rioux et al., 2012, 2013, 2016; Rioux, Garber, et al., 2021).

Several studies have further argued that the ophiolite likely formed during the initiation of an entirely new subduction zone. This model is supported by the similar stratigraphy observed in many ophiolites and the Izu–Bonin–Mariana (IBM) forearc, which has been attributed to subduction initiation. The observed stratigraphy in both settings includes a progression from lavas with compositions similar to mid-ocean ridge basalts (forearc basalts), to transitional compositions, and then the subsequent eruption of boninites (Reagan et al., 2010, 2017; Stern et al., 2012; Stern & Bloomer, 1992). In a recent study, Belgrano et al. (2019) compared compiled data from the IBM forearc and the Samail ophiolite and concluded that the similar geochemical progression in both settings support formation of the ophiolite during subduction initiation, albeit with distinct mantle and slab compositions between the two localities. The identification of boninite lavas within the V2 lavas series of the ophiolite (Ishikawa et al., 2002; Kusano et al., 2014, 2017)—which are typical of early arc environments—further supports formation of the ophiolite during subduction initiation. The thermal history of the metamorphic sole, with *P–T* conditions that are hotter than average subduction zone geotherms, also broadly suggests a juvenile subduction zone (Agard et al., 2020; Cowan et al., 2014; Ghent & Stout, 1981; Gnos, 1998; Hacker & Mosenfelder, 1996; Holt & Condit, 2021; Peacock, 1991, 1996; Searle & Malpas, 1980; Soret et al., 2017; Syracuse et al., 2010; Zhou & Wada, 2021). Finally, the temporal progression of Samail ophiolite magmatism matches those observed in the IBM forearc during subduction initiation (Rioux et al., 2013; Rioux, Garber, et al., 2021).

### 2.2 | The metamorphic sole

The metamorphic sole of the Samail ophiolite consists of a thin (tens to hundreds of m thick) layer of granulite- to



greenschist-facies metabasalts and metasediments located along the base of the ophiolite (Figure 1). The sole is exposed in several localities along the margins of the ophiolite (Gnos, 1992; Nicolas et al., 2000; Searle & Cox, 2002; Searle & Malpas, 1980, 1982), with the best-studied sections at the Wadi Tayin (Oman), Sumeini (Oman) and Masafi (UAE) localities (Figure 1). At each exposure, the sole is separated from the overlying mantle harzburgite by the Samail Thrust (Searle et al., 2022); where the highest grade sole rocks are exposed, they are juxtaposed across the thrust with a <1 m veneer of serpentinite overlain by a section of sheared, banded mantle harzburgites (Ambrose et al., 2018; Prigent, Agard, Guillot, Godard, & Dubacq, 2018; Prigent, Guillot, Agard, & Ildefonse, 2018; Prigent, Guillot, Agard, Lemarchand, et al., 2018). Below the thrust, sole exposures record condensed, inverted and imbricated metamorphic gradients, reflecting tectonic juxtaposition of rocks metamorphosed at different pressures and temperatures (Agard et al., 2016; Ambrose et al., 2021; Gnos, 1998; Soret et al., 2017). The highest grade rocks in the metamorphic sole consist of garnet-clinopyroxene amphibolites exposed in a narrow layer (~1–85 m thick) (Ambrose et al., 2021; Cowan et al., 2014; Ghent & Stout, 1981; Hacker & Mosenfelder, 1996; Searle & Cox, 2002; Searle & Malpas, 1980, 1982; Soret et al., 2017). In many sole localities, this high-grade layer is absent from the section, likely reflecting post-emplacement reactivation of the Samail thrust and excision of the highest grade rocks. The garnet amphibolites are sequentially underlain by lower grade, mostly garnet- and clinopyroxene-free amphibolites, followed by greenschist-facies mafic and metasedimentary rocks (Garber et al., 2020; Gnos, 1998; Hacker & Mosenfelder, 1996; Kotowski et al., 2021; Searle & Malpas, 1980; Soret et al., 2017). We adopt the nomenclature of Soret et al. (2017) and refer to the highest grade garnet- and clinopyroxene-bearing amphibolites exposed directly below the Samail thrust as the HTa unit; the underlying, lower grade, largely garnet- and clinopyroxene-free amphibolites as the HTb unit; and the low-grade, lowermost metabasalts and metasediments as the LT unit.

Pressure and temperature ( $P$ – $T$ ) estimates from the sole range from 700°C to 900°C and 0.8–1.3 GPa for granulite-facies mineral assemblages within the HTa amphibolites (Ambrose et al., 2021; Cowan et al., 2014; Gnos, 1998; Hacker & Mosenfelder, 1996; Soret et al., 2017); ~650–775°C and 0.7–0.9 GPa for the upper amphibolite-facies HTb mineral assemblages (Garber et al., 2020; Soret et al., 2017, 2019); and 480–580°C and 0.4–0.6 GPa for the LT lower amphibolite to greenschist-facies metasediments and metabasalts (Gnos, 1998; Hacker & Mosenfelder, 1996; Soret et al., 2017), although

recent work argues for higher peak pressures of 0.7–1 GPa in the LT sole, similar to the HT units (Kotowski et al., 2021). Peak  $P$  estimates from thermobarometry are consistent at the Masafi, Sumeini, Al Ajaiz and Wadi Tayin localities, which span the length of the ophiolite from north to south (Figure 1) (Cowan et al., 2014; Cox, 2000; Gnos, 1998; Searle & Cox, 2002; Soret et al., 2017). The package of high- to low-grade sole units are together thrust over low-grade to un-metamorphosed sedimentary and volcanic rocks of the Haybi and Hawasina complexes, consisting of Permian to Triassic deep-sea sediments, limestones and alkali basaltic seamounts (Searle, 1985; Searle et al., 1980).

Using data and observations primarily from the Sumeini Window, Soret et al. (2017) argued that the HTa, HTb and LT units form discrete, internally coherent thrust sheets, consistent with models linking the detachment of the sole to changes in rheology and plate coupling in a subducting slab (Agard et al., 2020, 2016). Alternately, evidence primarily from Wadi Tayin suggests a semi-continuous thermal gradient in the sole away from the Samail thrust, which may in turn indicate that the sole is composed of numerous, thinner thrust slices (Garber et al., 2020; Hacker & Mosenfelder, 1996).

The metamorphic sole was originally attributed to metamorphism as the ophiolite was thrust over adjacent oceanic lithosphere; however, because the peak metamorphic pressures in the sole of 1.0–1.3 GPa correspond to lithostatic depths of 30–40 km, the pressures are too high to be explained by the current thickness of the lithospheric section of the ophiolite (15–20 km) (Ambrose et al., 2021; Cowan et al., 2014; Gnos, 1998; Hacker & Gnos, 1997). Further, there appear to be systematic chemical differences between the metamorphic sole amphibolites and the ophiolite lavas, with the sole amphibolites characterized by higher Cr and higher light rare earth element/heavy rare earth element (LREE/HREE) ratios (Godard et al., 2006, 2003; Ishikawa et al., 2005; Kusano et al., 2012, 2014, 2017; Searle & Malpas, 1982). These observations support the interpretation that the metamorphic sole is a preserved remnant of a subducted slab.

## 2.3 | Existing temporal constraints

Previous geochronology from the ophiolite and metamorphic sole includes U–Pb, K–Ar and Lu–Hf dating (e.g., Goodenough et al., 2010; Guilmette et al., 2018; Hacker et al., 1996; Rioux et al., 2016; Styles et al., 2006; Tilton et al., 1981; Warren et al., 2005). Zircon, titanite and monazite U–Pb and garnet-whole rock Lu–Hf isochron dates are interpreted to reflect the timing of

mineral growth or recrystallization within the ophiolite crust and metamorphic sole, whereas hornblende  $^{40}\text{Ar}/^{39}\text{Ar}$  dates reflect the timing of cooling of the crust and sole below  $\sim 500\text{--}550^\circ\text{C}$  (Cherniak et al., 2004; Cherniak & Watson, 2001; Guilmette et al., 2018; Hacker et al., 1996; Harrison, 1982; Holder et al., 2019; Scherer et al., 2000; Soret et al., 2022). Here, we briefly summarize the existing temporal constraints, with an emphasis on U–Pb dates from our previous research, which provide a large, internally consistent dataset for comparison to the results reported herein.

The timing of crustal magmatism within the ophiolite has primarily been constrained through U–Pb zircon geochronology, including detailed studies by Tilton et al. (1981), Warren et al. (2005) and Styles et al. (2006). Building on these previous studies, we carried out extensive isotope dilution-thermal ionization mass spectrometry (ID-TIMS) U–Pb zircon dating along the length of the ophiolite in Oman and the UAE (Rioux et al., 2012, 2013, 2016; Rioux, Garber, et al., 2021). Our data indicate that plutonic rocks related to V1 magmatism crystallized from 96.1–95.6 Ma ( $n = 21$ ), followed by intrusion of plutonic rocks related to V2 magmatism from 95.6–95.2 Ma ( $n = 18$ ). Felsic dikes with low  $\varepsilon_{\text{Nd}}$  and  $\varepsilon_{\text{Hf}}$  and elevated  $\delta^{18}\text{O}$  (Amri et al., 2007; Haase et al., 2015; Rioux, Benoit, et al., 2021; Rollinson, 2014, 2015; Spencer et al., 2017)—which have been attributed to the subduction and melting of oceanic crust and sediment below the ophiolite—yield U–Pb dates from 95.2–95.0 Ma ( $n = 6$ ; excluding one older outlier) in the Oman portion of the ophiolite, while similar and more peraluminous intrusions in the UAE have younger dates of 94.1–91.0 Ma ( $n = 5$ ) (Rioux, Garber, et al., 2021).

In the metamorphic sole, K–Ar and  $^{40}\text{Ar}/^{39}\text{Ar}$  dating first demonstrated that cooling ages from the sole are similar to the timing of ophiolite magmatism (Gnos & Peters, 1993; Hacker et al., 1996; Montigny et al., 1988). Hacker et al. (1996) reported a large set of high-precision  $^{40}\text{Ar}/^{39}\text{Ar}$  dates from along the length of the ophiolite, demonstrating that hornblende cooling dates from the metamorphic sole ranged from  $95.7 \pm 0.6$  to  $92.6 \pm 1.2$  Ma, overlapping hornblende cooling dates from plutonic rocks in the ophiolite crust and mantle of  $96.3 \pm 2.6$  to  $93.3 \pm 1.0$  Ma ( $\pm 2\sigma$ ). The authors interpreted the data to reflect rapid formation and cooling of the metamorphic sole after formation of the ophiolite.

Warren et al. (2005) and Styles et al. (2006) further reported ID-TIMS U–Pb zircon dates from the Wadi Tayin ( $94.48 \pm 0.23$  Ma;  $n = 2$ ) and Masafi ( $95.29 \pm 0.21$  to  $95.69 \pm 0.25$  Ma;  $n = 2$ ) sole localities, respectively—these dates are reported as in the original studies, with no Th correction. We subsequently carried out ID-TIMS U–Pb zircon dating on samples from the Sumeini and

Wadi Tayin localities (Rioux et al., 2013, 2016; Rioux, Garber, et al., 2021). Two leucocratic pods from the Sumeini sole locality yielded Th-corrected  $^{206}\text{Pb}/^{238}\text{U}$  weighted mean dates of  $96.169 \pm 0.022$  Ma (13213M05) and  $96.146 \pm 0.035$  Ma (13213M06), and a third, texturally cross-cutting dyke yielded a younger date of  $95.28 \pm 0.24$  Ma (13213M02). Two leucocratic pods from the Wadi Tayin sole locality yielded weighted mean dates of  $94.815 \pm 0.030$  Ma (13222M02) and  $94.69 \pm 0.11$  Ma (CWO14), while a garnet amphibolite sample yielded a range of dates from  $96.067 \pm 0.068$  to  $95.085 \pm 0.063$  Ma (13222M08, redated in this study). We also dated an additional amphibolite sample from the Bani Hamid section in the UAE—an out of sequence thrust sheet of metamorphic rocks within the mantle section—which yielded a date of  $94.51 \pm 0.12$  Ma (Searle et al., 2015). Kim et al. (2020) reported laser-ablation inductively coupled mass spectrometry (LA-ICP-MS) U–Pb zircon dates from a single garnet amphibolite sample that range from 95.7–88.8 Ma, while Garber et al. (2020) reported LA-ICP-MS zircon rim dates from two zircon grains of 98.7–94.1 Ma from a metasediment within the garnet free-amphibolites.

In contrast to the range of metamorphic sole U–Pb dates that overlap with the overlying ophiolite, Guilmette et al. (2018) reported Lu–Hf garnet-whole rock isochron dates of  $104.1 \pm 1.1$  Ma to  $103.2 \pm 1.2$  Ma on garnet-clinopyroxene amphibolites from Sumeini ( $n = 1$ ) and Wadi Tayin ( $n = 2$ ). They also reported TIMS U–Pb zircon and titanite dates from one of their Wadi Tayin samples of  $96.19 \pm 0.14$  Ma and  $95.60 \pm 0.27$  Ma, respectively. The Lu–Hf isochron dates are significantly older than the U–Pb dates from the ophiolite crust and metamorphic sole and were attributed to metamorphism during an early phase of induced subduction initiation. The authors suggested that the younger zircon dates from both leucocratic pods and garnet amphibolite samples in the sole—from their study and previous work—reflect zircon crystallization from late, highly fractionated melts during retrograde cooling of the sole. In a separate study, we reported a Lu–Hf garnet-whole rock isochron date of  $93.0 \pm 0.5$  Ma from an HTb amphibolite-facies metasediment at Wadi Tayin, which we interpreted as the timing of peak metamorphism in lower grade rocks structurally beneath the garnet amphibolites (Garber et al., 2020).

Finally, Soret et al. (2022) reported in situ LA-ICP-MS titanite and monazite petrochronology from the metamorphic sole. Titanite from the highest grade garnet amphibolites yielded dates of 100–95 Ma. Depletion of the heavy rare earth elements and inclusion within garnet of the dated titanite were both attributed to

synchronous titanite and garnet growth during prograde metamorphism. Monazite from a metasedimentary rock from the HTb unit yielded similar dates of 99.5–96.6 Ma. Kotowski et al. (2021) reported LA-ICP-MS titanite U–Pb analyses from the low-temperature (LT) sole that are consistent with dates of ~95–90 Ma (based on the range of dates in their Table S5).

The existing data for the timing of prograde to peak metamorphism of the rocks below the ophiolite are inconclusive. Guilmette et al. (2018) interpreted the garnet-whole rock Lu–Hf isochron dates to reflect early metamorphism at ~104 Ma, whereas the zircon yield significantly younger U–Pb dates of ~96–95 Ma. Here, we present new coupled zircon U–Pb dates and trace element data that directly link zircon growth to prograde to peak metamorphism and clarify the timing of sole formation.

### 3 | METHODS

Zircon grains were separated using standard density and magnetic separation techniques and then mounted, polished to expose grain cores and imaged by cathodoluminescence (CL; Figure S1). Following imaging, coupled zircon trace-element analyses and reconnaissance U–Pb dating was carried out simultaneously by laser ablation split stream (LASS) at UC Santa Barbara (UCSB) (Kylander-Clark et al., 2013). Individual zircon grains were then selected and plucked out of the grain mounts

for high-precision chemical abrasion ID-TIMS U–Pb dating in the Isotope Geology Laboratory at Boise State University (BSU) (Mattinson, 2005). All TIMS analyses in this study were on either single zircon grains or grain fragments. We selected grains that spanned the range of chemical compositions observed in the LA-ICP-MS analyses for each sample and micro-sampled a subset of the dated grains to test for intra-grain age variations or to isolate chemically distinct cores and rims. During micro-sampling, the grains were either broken by hand or cut with a laser (Figures 2 and S2–S4) (Crowley, 2018; Kovacs et al., 2020), and resulting fragments were individually dated. TIMS data were reduced using the Tripoli and ET\_Redux programs (Bowring et al., 2011; McLean et al., 2011). Reported uncertainties on Th-corrected  $^{206}\text{Pb}/^{238}\text{U}$  dates are internal errors only, because this study is primarily focused on comparing (1) the relative timing of zircon grains with different chemical compositions within individual samples and (2) the relative timing of U–Pb dates from the metamorphic sole to U–Pb dates from the ophiolite crust. For context, a sample with internal uncertainties of  $\pm 0.03$  Ma has internal + tracer uncertainties of  $\pm 0.05$  Ma and internal + tracer + decay constant uncertainties of 0.11 Ma. Following the TIMS analyses, the Hf isotopic compositions of remaining zircon grains were analysed by laser ablation at UCSB. To understand the rock-wide trace element budget of the garnet amphibolites in the metamorphic sole, we also analysed the trace element compositions of garnet, amphibole, clinopyroxene, plagioclase and titanite from

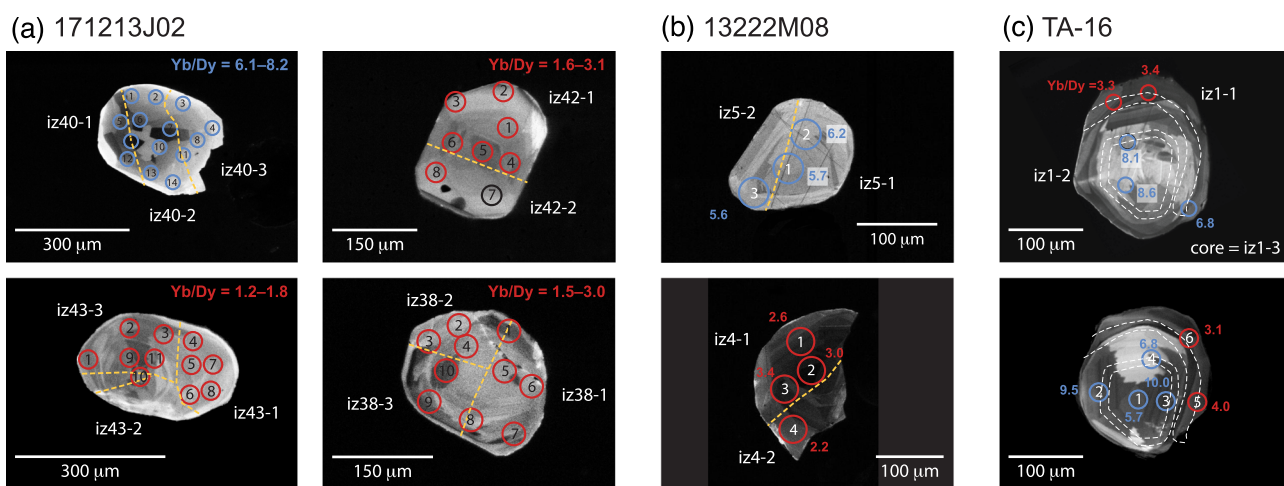


**FIGURE 2** Cathodoluminescence images of micro-sampled zircon grains. (a, b) Grains were broken into multiple pieces along yellow dashed lines. (c) Example of a laser milled grain (Figure S2). The top and lower panels are CL from the front and back side of an ~30  $\mu\text{m}$  thick polished wafer of grain iz1. The white dashed lines show the laser cut. In all panels, blue spots have Yb/Dy > 5, red spots have Yb/Dy < 5, black spots have Yb/Dy with high uncertainties and white fragment numbers (e.g., iz40-1) correspond to ID-TIMS fragment dates in Table S2 and Figure 5. Numbers within the spots are the spot numbers (Table S1), and red and blue numbers beside spots are the measured Yb/Dy. Spot Yb/Dy is not included for zircon grains from 171213J02, but the grains do not show any zoning with respect to Yb/Dy. All other micro-sampled grains are shown in Figures S2–S4.

several samples by LA-ICP-MS at UCSB and The Pennsylvania State University (PSU). Detailed analytical procedures for the zircon and major phase analyses are provided in the supporting information.

## 4 | RESULTS

### 4.1 | Sample description

In this study, we focus on three different lithologies from metamorphic sole outcrops along the length of the ophiolite: garnet-clinopyroxene amphibolites, garnet-free

amphibolites and leucocratic pods within the amphibolites (Figure 1 and Table 1). The highest grade, garnet-clinopyroxene amphibolite samples come from directly below the Samail thrust and represent the HTa unit. We tentatively also include a garnet-free, clinopyroxene-bearing amphibolite in the HTa unit based on its U–Pb date (171218M04). Four other garnet-free amphibolites are from structurally lower in the sole, representing the lower grade HTb unit—only one of these samples contains clinopyroxene (13OJG12). The HTb unit is defined by the presence of cm- to m-scale mineralogical banding, reflecting variations in the modal proportion of plagioclase + amphibole (Soret et al., 2017). In this context,

TABLE 1 Sample locations and descriptions.

| Sample                | UTM (E) <sup>a</sup> | UTM (N) <sup>a</sup> | IGSN <sup>b</sup> | Location      | Rock type                 | Unit | $\epsilon_{\text{Hf}}(96 \text{ Ma})^c$ |
|-----------------------|----------------------|----------------------|-------------------|---------------|---------------------------|------|---|
| <b>Oman</b>           |                      |                      |                   |               |                           |      |   |
| 13222M08              | 663,609              | 2,550,565            | MER302228         | Wadi Tayin    | Garnet amphibolite        | HTa  | 10.6                                    |
| 13OJGWT15             | 664,128              | 2,551,290            | MER13JG15         | Wadi Tayin    | Garnet amphibolite        | HTa  | 8.4 <sup>d</sup>                        |
| 13223M02 <sup>e</sup> | 657,288              | 2,555,452            | MER132302         | Hammah Window | Leucocratic pod           | –    | 11.5                                    |
| 171213M01             | 657,956              | 2,555,558            | MER171301         | Hammah Window | Leucocratic pod           | –    | 9.8                                     |
| 171213M08             | 657,614              | 2,555,401            | MER171308         | Hammah Window | Amphibolite               | HTb  | 6.5                                     |
| 171213J02             | 657,286              | 2,555,486            | MER1713J2         | Hammah Window | Garnet amphibolite        | HTa  | 13.3                                    |
| 13OJG12               | 591,309              | 2,522,999            | MER13JG12         | Samail South  | Clinopyroxene amphibolite | HTb  |   |
| 181211M01             | 617,296              | 2,591,612            | MER181101         | Fanja         | Garnet amphibolite        | HTa  | 10.8                                    |
| 181212M01             | 626,900              | 2,582,008            | MER181201         | Fanja         | Garnet amphibolite        | HTa  | 13.1                                    |
| 171218M04             | 429,924              | 2,652,616            | MER171804         | Asjudi        | Clinopyroxene amphibolite | HTa  |   |
| 171218M10             | 420,894              | 2,656,627            | MER171810         | Asjudi        | Amphibolite               | HTb  | 11.7                                    |
| 181212M07             | 591,509              | 2,600,158            | MER181207         | Al Ajaiz      | Garnet amphibolite        | HTa  | 10.3                                    |
| 181212M10             | 589,291              | 2,596,216            | MER181210         | Al Ajaiz      | Garnet amphibolite        | HTa  | 11.7 <sup>d</sup>                       |
| 171219M06             | 406,279              | 2,726,158            | MER171906         | Sumeini       | Garnet amphibolite        | HTa  | 10.0                                    |
| 171219M09             | 399,589              | 2,731,731            | MER171909         | Sumeini W     | Garnet amphibolite        | HTa  | 11.3                                    |
| 171219M12             | 399,859              | 2,731,697            | MER171912         | Sumeini W     | Amphibolite               | HTb  |   |
| 13OJGSW01             | 406,443              | 2,731,917            | MER13JG01         | Sumeini       | Garnet amphibolite        | HTa  | 8.9                                     |
| <b>UAE</b>            |                      |                      |                   |               |                           |      |   |
| 181219M03             | 409,138              | 2,814,713            | MER181903         | Masafi NW     | Garnet amphibolite        | HTa  | 10.6                                    |
| 181219M13             | 408,855              | 2,814,711            | MER181913         | Masafi NW     | Garnet amphibolite        | HTa  | 9.6                                     |
| 181220M07             | 415,168              | 2,801,034            | MER182007         | Masafi S      | Garnet amphibolite        | HTa  | 10.6                                    |
| 181221M07             | 410,230              | 2,814,388            | MER182107         | Masafi E      | Garnet amphibolite        | HTa  | 9.8                                     |
| 181221M04             | 417,500              | 2,804,887            | MER182104         | Masafi E      | Garnet amphibolite        | HTa  | 14.6                                    |
| TA-16                 | 415,117              | 2,801,138            | MER15TA16         | Masafi S      | Garnet amphibolite        | HTa  | 10.0                                    |
| TA-72                 | 415,164              | 2,799,697            | MER15TA72         | Masafi S      | Garnet amphibolite        | HTa  | 9.8                                     |
| TA-84                 | 417,390              | 2,804,958            | MER15TA84         | Masafi E      | Garnet amphibolite        | HTa  | 10.0                                    |

<sup>a</sup>WGS 84, UTM zone 40.

<sup>b</sup>Assigned international geo sample number (IGSN).

<sup>c</sup>Age corrected  $\epsilon_{\text{Hf}}$  from Table S2.

<sup>d</sup>Weighted mean for 181212M10 for spots with  $\epsilon_{\text{Hf}}(t) > 0$ . 13OJGWT15 has a range of  $\epsilon_{\text{Hf}}(t)$  (see text).

<sup>e</sup>This sample is from the same pod as 171213M10, which Kelemen et al. (2022) dated by Th–U/He.



three samples come from outcrops with interlayered melanocratic (amphibole + epidote + titanite) and leucocratic (plagioclase + amphibole + epidote + titanite) bands (171213M08, 171218M10 and 171219M10), while the context of the final sample is not well constrained due to limited outcrop (13OJG12). For conciseness, we will refer to the garnet-clinopyroxene bearing amphibolites as ‘garnet amphibolites’ and those without garnet (with or without clinopyroxene) as ‘garnet-free amphibolites’ throughout. The dated leucocratic pods occur as cm-thick, cm- to m-long intrusions within garnet-free amphibolites either at the base of the HTa unit or within the HTb unit. The two dated pods are roughly parallel to foliation, although sample 171213M01 is from a network of veins, which cut foliation in some places. Similar pods in the HTa and HTb amphibolites have previously been attributed to partial melting of the amphibolites during metamorphism (Cowan et al., 2014; Rioux et al., 2016; Searle & Cox, 1999; Searle & Malpas, 1980, 1982; Soret et al., 2017). These leucocratic pods probably do not record primary melts, but rather cumulus fractions of melts whose liquids percolated upwards into the mantle section of the ophiolite (Rioux et al., 2016).

## 4.2 | Zircon trace element data

To characterize the zircon trace-element record in the studied samples, we performed ~3,000 laser ablation spot analyses on zircon grains from 25 samples (Figures 3–5 and S5; Table S1). For plotting and interpretation, we filtered data for each element to those analyses with  $2\sigma$  analytical uncertainties  $\leq 30\%$ ; all plots and discussion hereafter are based on these filtered data. All analysed zircon grains are HREE enriched and generally have positive Ce anomalies (Figure 3), although chondrite-normalized HREE slopes vary systematically with sample lithology. Throughout this manuscript, we will quantify the HREE slope using the unnormalized Yb/Dy ratio, where high Yb/Dy corresponds to zircon with steep HREE slopes, and low Yb/Dy corresponds to zircon with shallower HREE slopes (Figure 3). These Yb/Dy changes can theoretically arise from differences in Dy (middle rare earth element, MREE) or Yb (HREE), but changes in this ratio in our data primarily relate to variations in Yb (Figures 5 and S5), which we attribute to partitioning of the HREE between garnet and zircon.

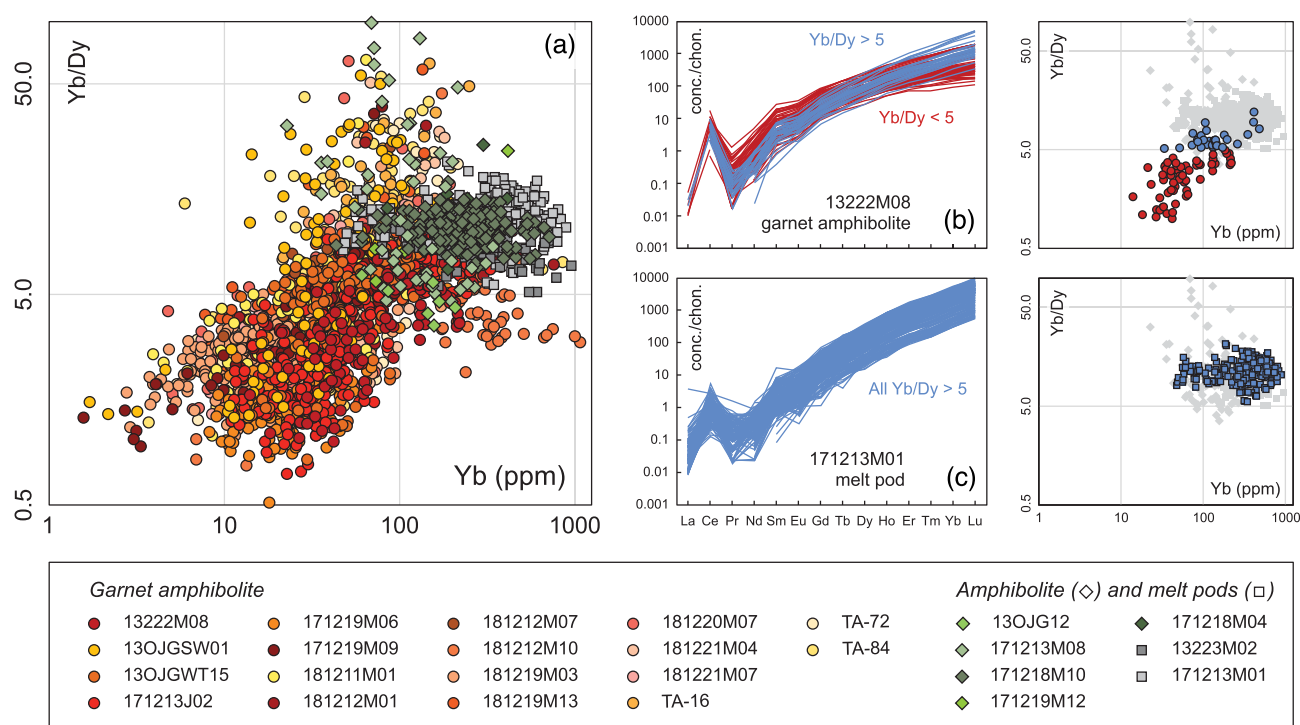


**FIGURE 3** Rare earth element (REE) characteristics of analysed zircon grains. (a) Yb concentration (ppm) versus unnormalized Yb/Dy. Zircon from garnet-free amphibolites (green) and melt pods (grey) have consistent, steep heavy REE slopes (Yb/Dy > 5). Garnet amphibolites (warm colours) have a range from steep (Yb/Dy > 5) to shallow (Yb/Dy < 5) heavy REE slopes. A single datum from 13OJGSW01 plots off scale at Yb/Dy < 0.5. Inherited grains (>300 Ma) in sample 181212M10 are excluded. Individual plots for each sample are provided in Figures 4 and 5. (b and c) Chondrite normalized REE plots and Yb versus unnormalized Yb/Dy plots showing the different REE patterns in zircon grains from a garnet amphibolite (13222M08; b) and a felsic melt pod (171213M01; c). Grey data points in (b) and (c) are the field of zircon data from non-garnet bearing amphibolites and leucocratic pods.

## Garnet-free amphibolites and leucocratic pods

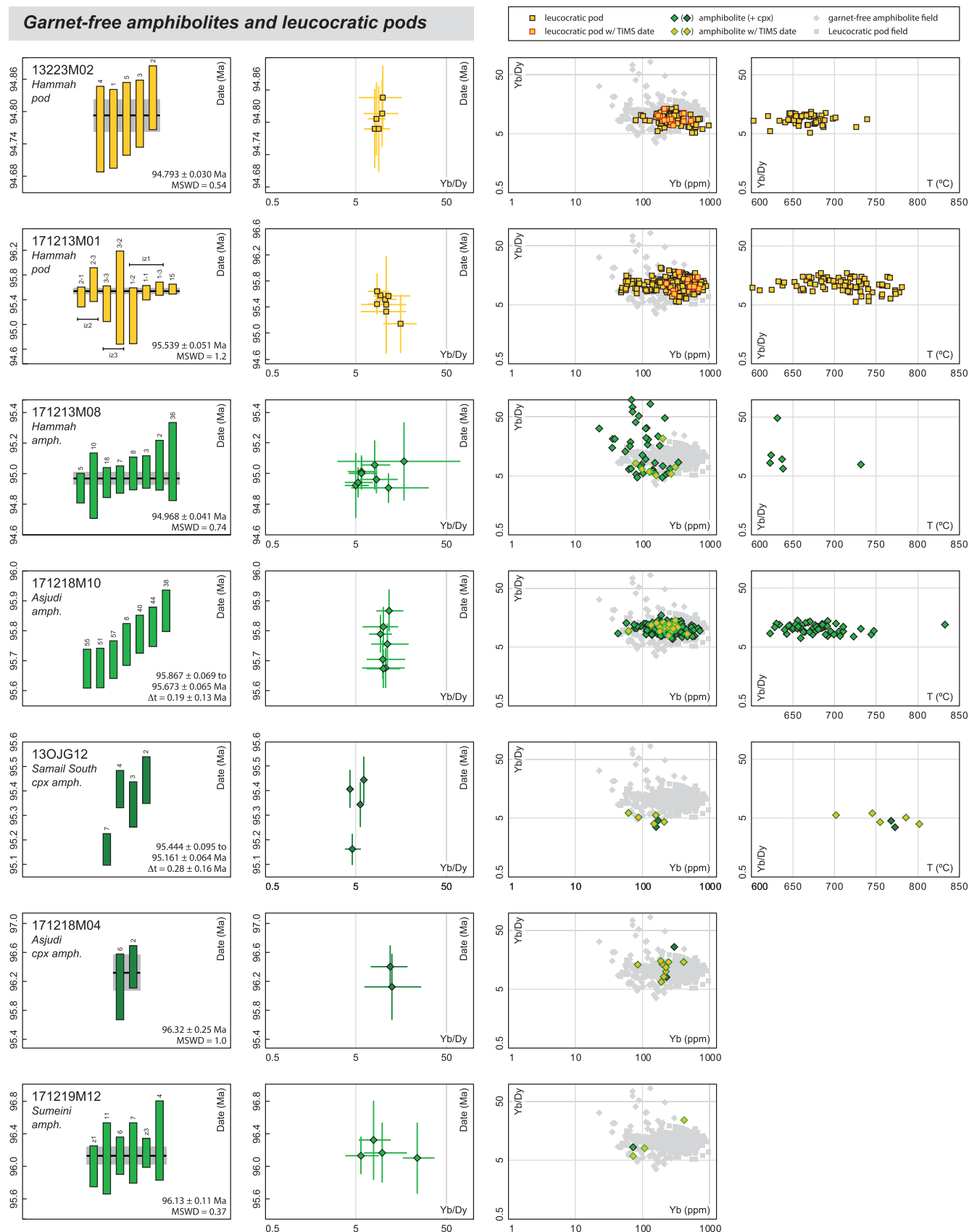


**FIGURE 4** Zircon trace element and isotope dilution-thermal ionization mass spectrometry (ID-TIMS) U-Pb data for the garnet-free amphibolites and leucocratic pods dated in this study. Darker green data points are clinopyroxene bearing garnet-free amphibolites. See the Figure 5 caption for details.

Garnet-free lithologies, including two leucocratic pods (13223M02 and 171213M01) and five garnet-free amphibolite samples (171213M08, 171218M04, 171218M10, 171219M12 and 13OJG12), have consistently steep HREE with  $\text{Yb/Dy} > 5$  ( $n = 586$ ; six spots have lower  $\text{Yb/Dy} = 3.5\text{--}4.6$ ; Figures 3 and 4). Three of these samples yield tightly clustered HREE slopes with  $\text{Yb/Dy} = 5.1\text{--}21.0$  and define horizontal arrays on plots of Yb versus Yb/Dy (13223M02, 171213M01 and 171218M10). Data from a fourth sample (171213M08) extend to steeper HREE slopes ( $\text{Yb/Dy} = 4.6\text{--}96.4$ ). The final three garnet-free amphibolite samples (13OJG12, 171218M04 and 171219M12) yielded too few zircon grains to robustly characterize the trace element systematics.

In contrast, garnet amphibolite samples ( $n = 18$ ) consistently record a range in zircon HREE, from steep ( $\text{Yb/Dy} > 5$ ) to shallow ( $\text{Yb/Dy} < 5$ ) slopes (Figures 3 and 5). In each garnet-bearing sample, the high Yb/Dy analyses overlap the field of zircon data from garnet-free samples, but the data from zircon grains from garnet-bearing samples extend to much lower values ( $\text{Yb/Dy} < 5$ ). Analysed Yb/Dy ranges from 0.3–64.2 for the complete dataset, excluding two low outliers ( $n = 2,183$ ). The data from these samples have a positive slope on plots of Yb versus Yb/Dy (i.e., decreasing Yb with decreasing Yb/Dy), in contrast to the horizontal arrays of the garnet-free samples. As discussed below, one sample (181212M10) contains a significant fraction of inherited zircon grains ( $\sim 1980\text{--}370$  Ma), and the trace element data from these grains are shown in grey in Figure 5.

### 4.3 | Zircon U–Pb data

Following trace-element analyses, individual zircon grains that spanned the range of observed compositions in each sample were plucked from the grain mounts and dated by ID-TIMS (Table S2). We analysed a total of 202 single grains or grain fragments (Table S2; Figures 4 and 5). All dates reported herein are Th-corrected  $^{206}\text{Pb}/^{238}\text{U}$  dates, which are the most precise and accurate dates for Cretaceous samples; most data points are either concordant or plot slightly to the right of concordia (higher  $^{207}\text{Pb}/^{235}\text{U}$ ), potentially reflecting excess  $^{207}\text{Pb}$  from initial incorporation of  $^{231}\text{Pa}$  (e.g., Rioux et al., 2015). We interpret data to represent a single population if the reduced chi-squared statistic (mean square of the weighted deviates, MSWD) falls within the calculated 95% confidence interval for the number of analysed fractions (Wendt & Carl, 1991).

Dated fractions from the two leucocratic pod samples define single populations, with weighted mean dates of  $95.539 \pm 0.051$  and  $94.793 \pm 0.030$  Ma (Figure 4). Three of the five garnet-free amphibolite samples also yield

single-population dates, with weighted means of  $96.32 \pm 0.25$  to  $94.968 \pm 0.041$  Ma. Two additional garnet-free amphibolite samples (171218M10 and 13OJG12) have a spread in single-grain dates from  $95.867 \pm 0.069$  to  $95.673 \pm 0.063$  Ma and  $95.444 \pm 0.095$  to  $95.161 \pm 0.064$  Ma, respectively.

Precise single-grain dates from 18 garnet amphibolite samples range from  $96.698 \pm 0.094$  to  $95.161 \pm 0.064$  Ma (Figure 5; excluding eight overlapping dates with  $2\sigma > 0.1$  Ma). In 11 samples, zircon grains or grain fragments with  $\text{Yb/Dy} > 5$  (blue in Figure 5) yield dates older than or within uncertainty of grains or grain fragments with  $\text{Yb/Dy} < 5$  (red in Figure 5) from the same sample (Group A samples in Figure 5). For each of these samples, the weighted mean date for zircon fractions with  $\text{Yb/Dy} > 5$  is systematically older than the weighted mean date of the  $\text{Yb/Dy} < 5$  zircon fractions. In 9 of the 11 samples, one or more of the zircon fractions with  $\text{Yb/Dy} > 5$  is older than one or more of the zircon fractions with  $\text{Yb/Dy} < 5$ , outside of uncertainty, while the converse is not observed. The variability in dates within individual samples ranges across the sample suite, with all analyses overlapping within uncertainty for some samples, whereas others have a spread of up to  $0.98 \pm 0.52$  Myr. A single additional sample (TA-72) was not amenable to dating of any  $\text{Yb/Dy} > 5$  zircon fragments due to low U and Pb concentrations, but the low Yb/Dy ( $< 5$ ) grains and grain fragments in this sample yield a range of dates from  $96.35 \pm 0.23$  to  $95.34 \pm 0.15$  Ma.

The zircon U–Pb systematics of the six remaining garnet amphibolite samples are more variable (Group B samples in Figure 5). Four samples (181211M01, 181212M10, 181221M07 and 13222M08) contain one or more older fraction(s) with  $\text{Yb/Dy} > 5$ , additional fractions with  $\text{Yb/Dy} < 5$  that either overlap within uncertainty or are younger than the high Yb/Dy fraction(s), followed by one or more younger fraction(s) with higher Yb/Dy. These samples define a counterclockwise pattern from older to younger dates on plots of Yb/Dy versus date (Figure 5, second column from left; poorly defined for 181221M07). For samples 181211M01, 181212M10 and 181221M07, the youngest, high Yb/Dy fractions have  $\text{Yb/Dy} > 5$ , whereas for sample 13222M08, the two youngest fractions do not reach  $\text{Yb/Dy} > 5$ . For sample 181212M10, the preliminary dating by LA-ICP-MS identified a large population of inherited zircon with dates of  $\sim 1980\text{--}370$  Ma (Table S1), and we focused on the  $\sim 96$  Ma population in our TIMS analyses. Two final samples (181212M01 and 181219M13) have a range of dates without any clear trend in Yb/Dy.

To identify and characterize any grain-scale age variations, we micro-sampled individual zircon grains from several samples. For samples 171213J02, 13222M08,

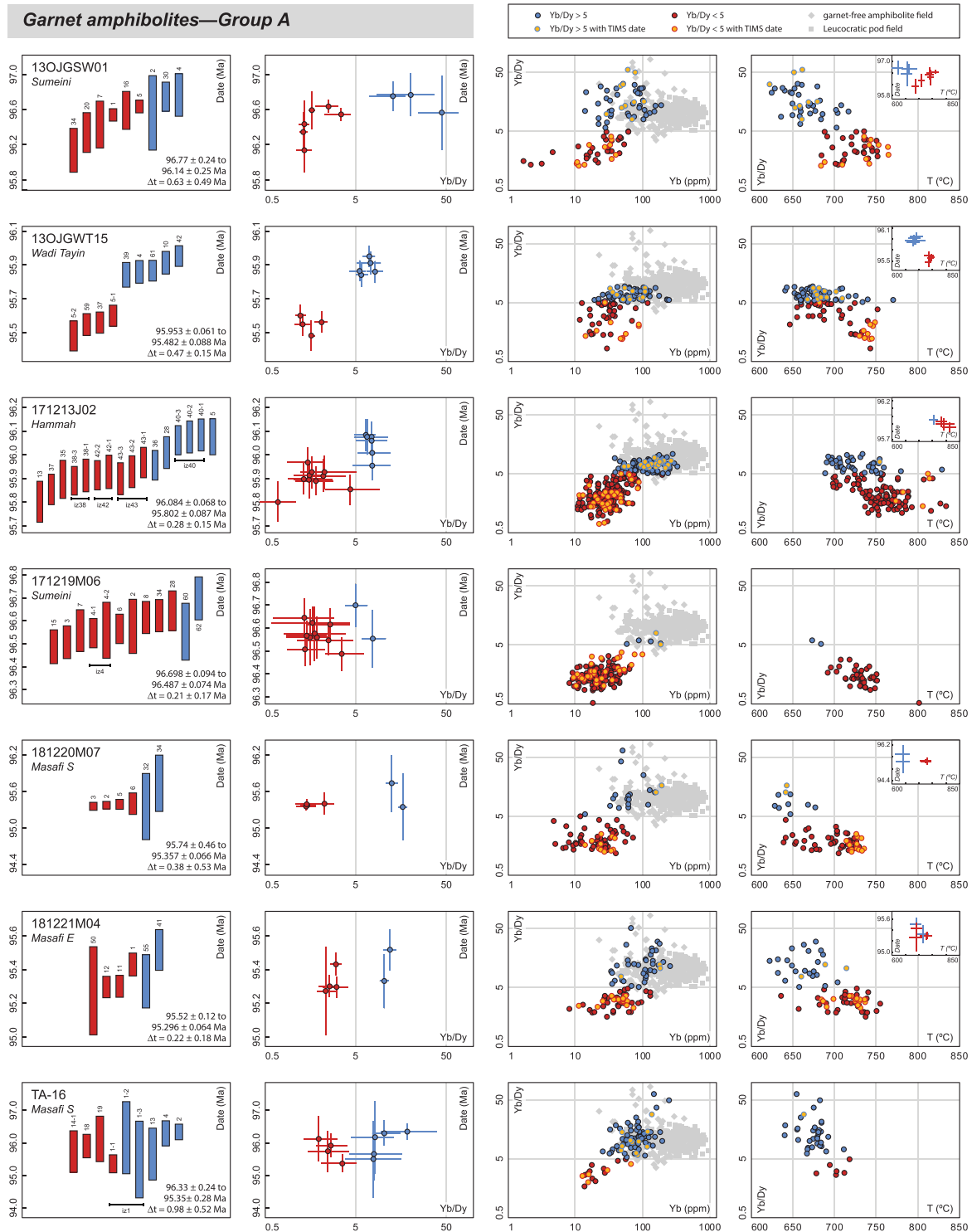


**FIGURE 5** Zircon trace element and isotope dilution-thermal ionization mass spectrometry (ID-TIMS) U–Pb data for the 18 garnet amphibolite samples dated in this study. Data are divided into Groups A and B analyses, as described in the text. Samples are ordered to highlight different data patterns. First column: ID-TIMS U–Pb dates. Second column: unnormalized Yb/Dy versus ID-TIMS date—plots symbols show the average Yb/Dy and x-axis error bars show the range of Yb/Dy, including 2σ uncertainties, from all of the spots on a dated grain. Third column: Yb (ppm) versus unnormalized Yb/Dy—the grey data show the range of data in garnet-free amphibolites and leucocratic pods from this study. Fourth column: Ti-in-zircon temperature versus unnormalized Yb/Dy, with inset showing Ti-in-zircon temperature versus ID-TIMS date; for the inset plots the error bars cross at the average Ti-in-zircon temperature and the x-axis error bars show the range of temperatures, including 2σ analytical only uncertainties, from all of the spots on a dated grain. A limited number of data points were excluded or plot of scale, as outlined in the supporting information.



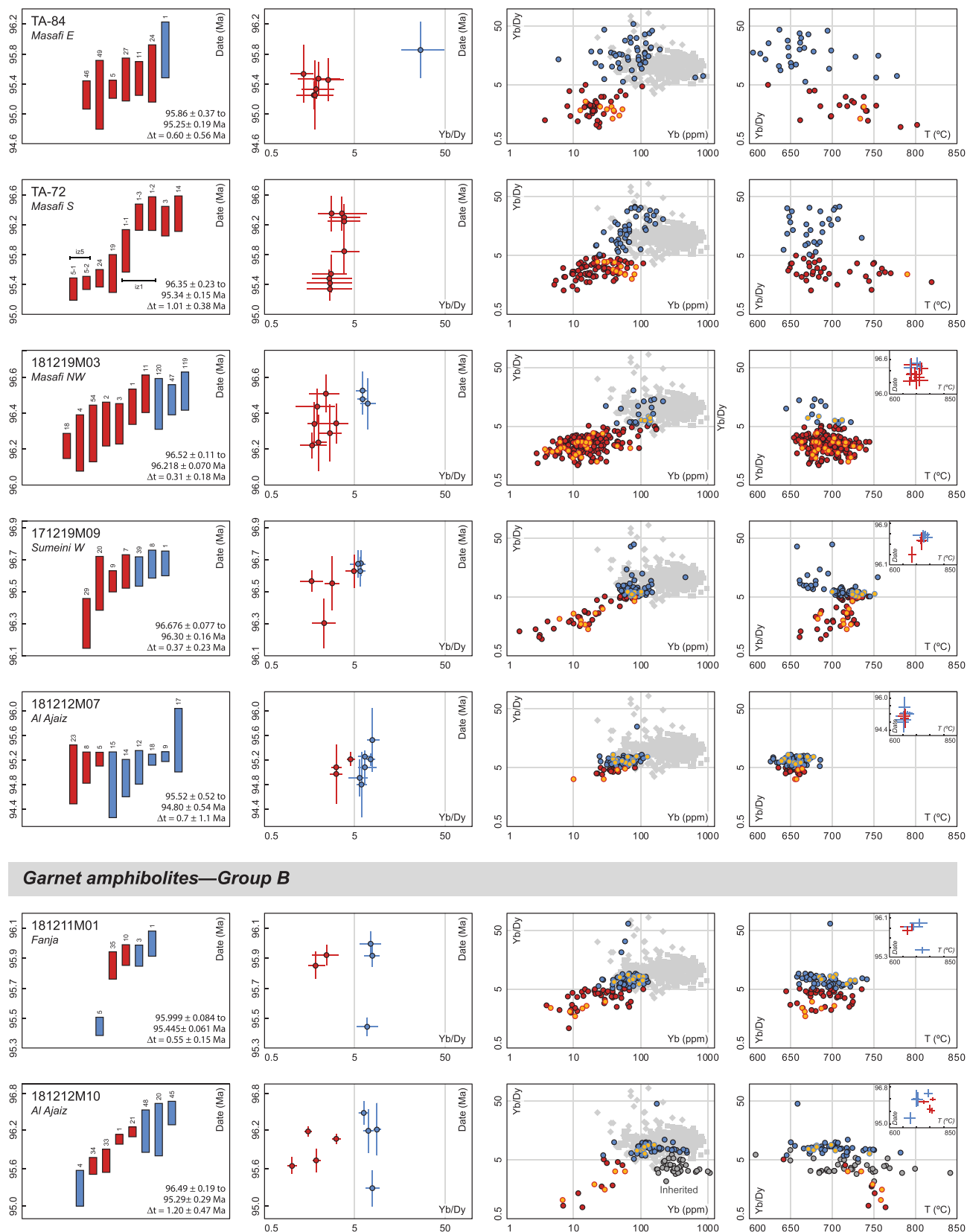


FIGURE 5 (Continued)

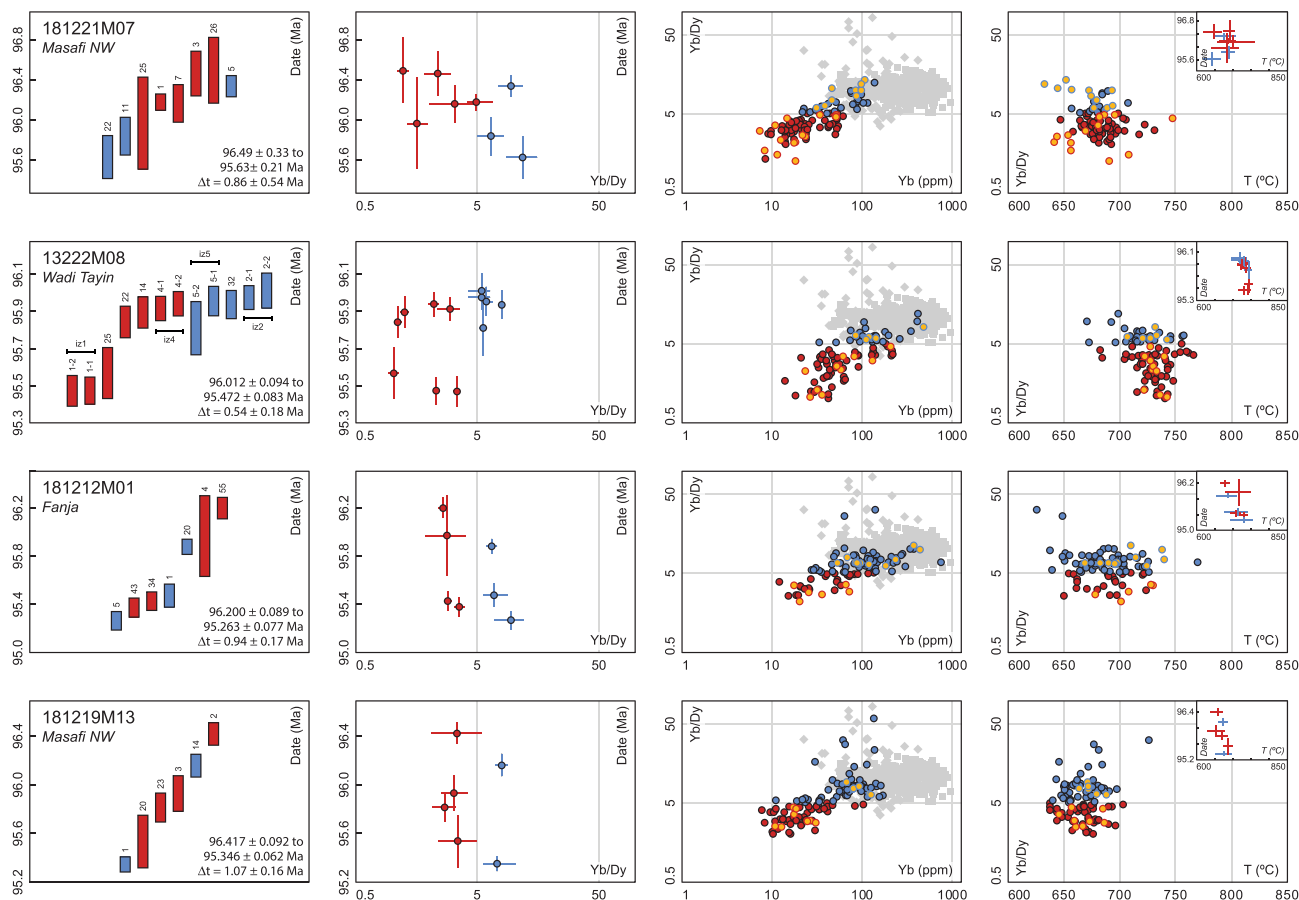


FIGURE 5 (Continued)

171213M01 and TA-72, the laser ablation analyses indicate that individual sector- to oscillatory-zoned zircon grains generally have uniformly high (>5) or low (<5) Yb/Dy (Figures 2, S1 and S4). To critically assess whether large grains with uniform Yb/Dy from these samples also have uniform dates, we broke grains into two to three fragments, then dated each fragment separately (all micro-sampled grains are shown in Figures 2 and S2–S4). In each case, the dates of the micro-sampled fragments agree within uncertainty (grain fragments labelled in the leftmost column of Figure 5), suggesting that single-grain dates provide a robust determination of the zircon crystallization age and do not reflect physical mixtures between older cores and younger rims. In sample TA-16, we identified grains with high Yb/Dy (> 5) cores overgrown by low Yb/Dy (< 5) rims. To date both the high Yb/Dy and low Yb/Dy zircon growth, we used laser milling to cut the grains (Figures 2, S2 and S3). For zircon iz1, we cut the grain to isolate a high Yb/Dy core, low Yb/Dy rim and a mixed zone in between (Figures 2 and S2). The dates for all three fragments overlap within uncertainty, indicating the transition from high to low Yb/Dy zircon occurred within the resolution of the relatively imprecise U–Pb

dates (~2.2 Ma); the dates from the rim and intermediate zone are low precision (±1.1–1.2 Ma) due to very low Pb contents and the small volume of dissolved zircon. For zircon iz14, we cut the grain into a rim fragment and mixed core-rim fragment. Only the rim fragment ran successfully, yielding a date of  $95.73 \pm 0.064$  Ma.

Our previous U–Pb dating from the ophiolite (Rioux et al., 2012, 2013, 2016; Rioux, Garber, et al., 2021) was carried out in the Isotope Laboratory at the Massachusetts Institute of Technology (MIT), whereas the dating for this study was performed in the Isotope Geology Laboratory at Boise State University. Repeat analyses of the EARTHTIME calibration solutions have shown good agreement between the two labs, and we used identical dissolution procedures and the same isotope tracer (ET535) in each study, such that any interlaboratory biases should be minimal. We additionally dated zircon from 13222M08 in both labs, providing an opportunity to compare the results. Single grain dates from our MIT analyses range from  $96.067 \pm 0.068$  to  $95.085 \pm 0.063$  Ma ( $n = 6$ ) (Rioux et al., 2016) compared to a range from  $96.012 \pm 0.094$  to  $95.472 \pm 0.083$  Ma ( $n = 12$ ) at BSU (this study). The data show good agreement between the labs,

recognizing that the range of zircon dates within this sample limits more detailed comparison.

#### 4.4 | Ti-in-zircon thermometry

Ti-in-zircon temperatures were calculated following Ferry and Watson (2007), using estimated  $a_{\text{TiO}_2}$  and  $a_{\text{SiO}_2}$  based on  $P$ – $T$  pseudosection modelling of sole amphibolite bulk compositions. For the prograde-to-peak  $P$ – $T$  conditions of the sole, and for two different average sole amphibolite major-element compositions from Ishikawa et al. (2005), pseudosections predict a total range of  $\sim 0.6$ – $1.0$  for both  $a_{\text{TiO}_2}$  and  $a_{\text{SiO}_2}$  (Figure S6). We adopted values of  $a_{\text{TiO}_2} = 0.75 \pm 0.25$  and  $a_{\text{SiO}_2} = 0.9 \pm 0.1$  in our calculations, reflecting the predicted range in garnet- and clinopyroxene-free amphibolites, which we consider to be the best estimate of the bulk composition of the garnet-clinopyroxene-bearing amphibolite protolith (Figure S6b), prior to high- $T$  metamorphism. Analytical uncertainties alone lead to  $2\sigma$  uncertainties on calculated Ti-in-zircon temperatures of  $\pm 5$ – $30^\circ\text{C}$  (plotted in Figure 5). Propagated analytical and activity uncertainties translate to uncertainties of  $\pm 50$ – $80^\circ\text{C}$ . In this study, we are primarily interested in relative changes in Ti-in-zircon temperatures, and as such, the absolute values of  $a_{\text{TiO}_2}$  and  $a_{\text{SiO}_2}$  are less important than changes in these values during metamorphism. We therefore plot data with only the analytical uncertainties in Figure 5 but discuss the potential impact of changing  $a_{\text{TiO}_2}$  and  $a_{\text{SiO}_2}$  below and in the supporting information.

Ti-in-zircon temperatures for zircon from leucocratic pods and garnet-free amphibolites range from  $\sim 590$ – $785^\circ\text{C}$ , excluding two high outliers, and do not show any

correlation with Yb/Dy (Figure 4). In the garnet amphibolites, Ti-in-zircon temperatures range from  $\sim 615$ – $830^\circ\text{C}$  (Figure 5). The analysed garnet amphibolite samples define two distinct trends with respect to Ti-in-zircon temperatures. Most of the samples in Group A in Figure 5—with the exception of 181219M03, 171219M09 and 181212M07—record a negative correlation between Ti-in-zircon temperatures and Yb/Dy, such that decreasing Yb/Dy correlates with increasing apparent crystallization temperature. For these samples, the average Ti-in-zircon temperature for spot analyses with Yb/Dy  $< 5$  is hotter than the average Ti-in-zircon temperature for spot analyses with Yb/Dy  $> 5$ , with an offset of  $24$ – $63^\circ\text{C}$  (Figures 5 and S7). In contrast, the remaining Group A and all Group B samples do not show a correlation between Ti-in-zircon temperature and Yb/Dy, and the range of Ti-in-zircon temperatures overlap for high and low Yb/Dy samples (Figures 5 and S7). On average, the samples with a correlation between Ti-in-zircon temperature and Yb/Dy record higher maximum temperatures, although there is overlap with samples lacking a correlation (Figure S7). The differing Ti versus Yb/Dy systematics do not define geographic trends; both data patterns are found along the length of the ophiolite and individual sole exposures contain examples of both groups (e.g., Wadi Tayin; Figure 1).

We used pseudosection modelling and comparison to previous work to assess whether  $a_{\text{TiO}_2}$  and  $a_{\text{SiO}_2}$  were likely to change during metamorphism (supporting information). These considerations suggest that it is unlikely that the observed variations in Ti-in-zircon temperatures reflect whole rock changes in  $a_{\text{TiO}_2}$  and/or  $a_{\text{SiO}_2}$  due to solid state metamorphic phase changes, but removal of partial melt during metamorphism could decrease the  $a_{\text{SiO}_2}$ . In this context, the increase in Ti-in-zircon temperature with decreasing Yb/Dy in most Group A samples

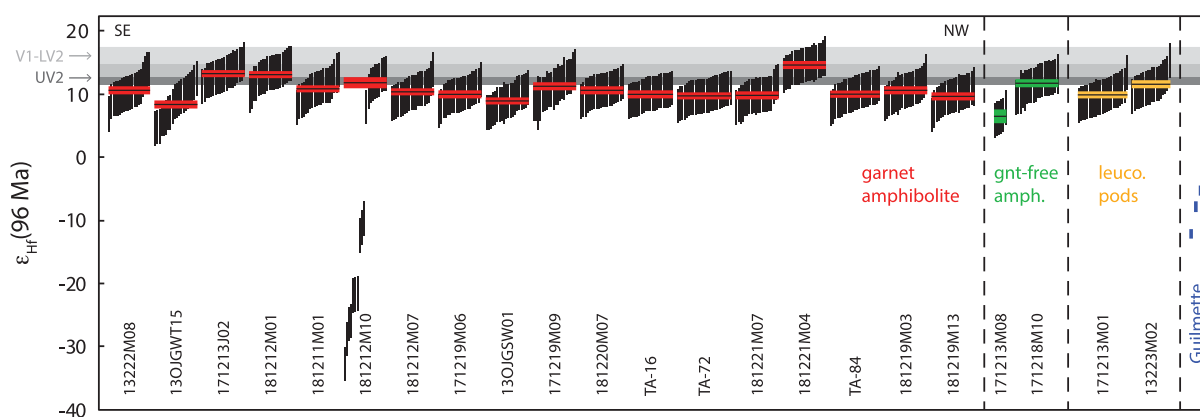


**FIGURE 6** Laser ablation-inductively coupled plasma-mass spectrometry (LA-ICP-MS) zircon  $\epsilon_{\text{Hf}}(t)$ . Vertical bars are spot data and thick black horizontal lines with coloured bands show weighted mean values, with  $2\sigma$  uncertainties. The weighted mean for 181212M01 is calculated for data with  $\epsilon_{\text{Hf}}(t) > 0$ . Samples are arranged from southeast to northwest. Leuco. pods, leucocratic pods; gnt-free amph., garnet-free amphibolite. Blue bars show the initial  $\epsilon_{\text{Hf}}(t)$  values from the Lu–Hf isochrons from Guilmette et al. (2018). Grey bands show the range of  $\epsilon_{\text{Hf}}(t)$  in V1 and V2 volcanic rocks from Kusano et al. (2017).

could reflect either a true increase in temperature at a constant  $a_{\text{SiO}_2}$  or a decrease in  $a_{\text{SiO}_2}$  at a relatively constant temperature.

#### 4.5 | Zircon Hf isotopic data

Nineteen of 22 analysed samples have weighted mean  $\varepsilon_{\text{Hf}}(t)$  of  $6.5 \pm 1.1$  to  $14.6 \pm 0.6$  (Figure 6; Table S3), with MSWD that are consistent with the data representing repeat measurements of a single value (Wendt & Carl, 1991). One additional sample (13222M08) has a weighted mean  $\varepsilon_{\text{Hf}}(t)$  of  $10.6 \pm 0.6$  with a slightly elevated MSWD = 1.68, likely reflecting minor excess analytical scatter. For these samples, we consider the weighted mean of the spot data as the best estimate of the initial Hf isotopic composition (Figure 6). In contrast, two samples have a larger range in measured Hf isotopic compositions that likely reflects true geologic scatter: sample 13OJGWT15 yields spot data with  $\varepsilon_{\text{Hf}}(t) = 4.5 \pm 2.7$  to  $12.5 \pm 2.8$  (MSWD of 3.3), and sample 181212M10 yields a more extreme range of  $\varepsilon_{\text{Hf}}(t) = -32.7 \pm 2.7$  to  $13.3 \pm 2.7$ . The isotopic data for the latter sample correlate with laser ablation U–Pb spot dates: analyses with  $\varepsilon_{\text{Hf}}(t) = -18.1$  to  $-9.7$  are from inherited zircon grains with spot dates of 1590–447 Ma, with lower  $\varepsilon_{\text{Hf}}(t)$  corresponding to older dates, while zircon with U–Pb dates of  $\sim 96$  Ma define a single population of Hf data with a weighted

mean  $\varepsilon_{\text{Hf}}(t) = 11.7 \pm 0.85$  ( $n = 10$ ; MSWD = 1.4). All reported  $\varepsilon_{\text{Hf}}(t)$  data are corrected to 96 Ma, including the inherited grains from 181212M10, to allow for comparison of the isotopic compositions at the time of sole metamorphism.

#### 4.6 | Trace element data from other metamorphic phases

Trace-element data from garnet, amphibole, clinopyroxene, plagioclase and titanite from garnet amphibolite samples from the metamorphic sole are reported in Table S4. Data from eight samples show consistent HREE systematics, in which clinopyroxene, amphibole and titanite have  $\text{Yb/Dy} < 1$  (Figure 7), with the exception of three anomalous, low-Yb clinopyroxene spots from a single sample (171214J01). Yb concentrations are low for clinopyroxene (0.1–5.1 ppm) and amphibole (1.5–9.9 ppm) but reach higher values for titanite (1.1–144.8 ppm). Garnet grains have the highest HREE slopes, with  $\text{Yb/Dy} = 0.4\text{--}5.1$ , and Yb concentrations of 0.5–76.9 ppm. Plagioclase analyses record uniformly low Yb concentrations ( $\leq 0.16$  ppm) and  $\text{Yb/Dy} < 1$ , with the exception of four anomalous spot analyses with  $\text{Yb/Dy} > 1$ . Of the analysed samples, 171214J01 had fresh plagioclase, while the plagioclase was altered and retrogressed in all other samples; however, altered and fresh plagioclase yielded similar trace element results.

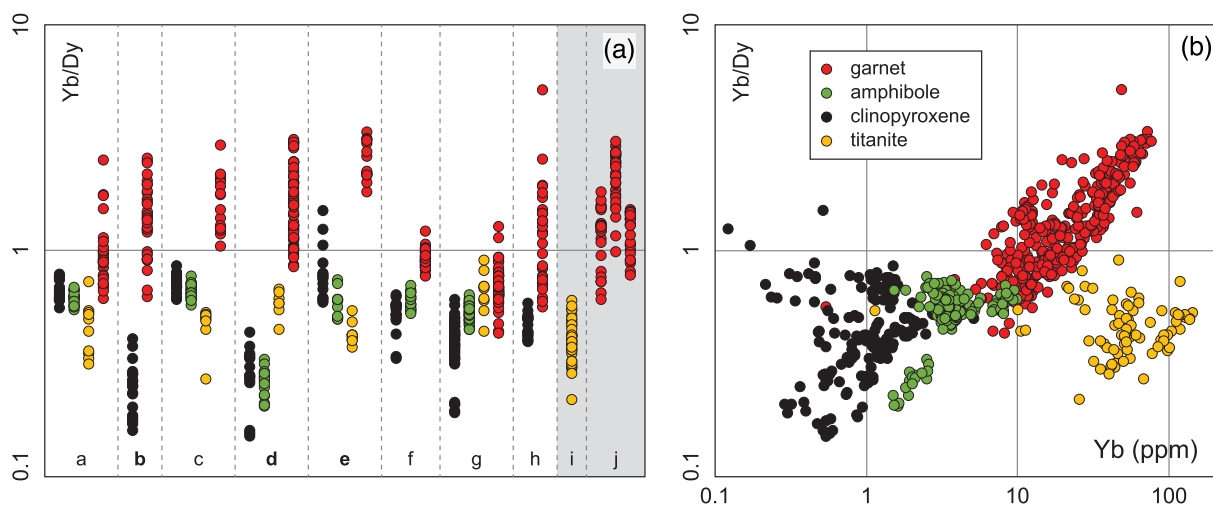


**FIGURE 7** (a) Yb/Dy of clinopyroxene, amphibole, titanite and garnet in sole garnet amphibolite samples. Letters in bold are samples dated in this study or are a sample from the same outcrop as a dated sample. Grey background denotes published data from Garber et al. (2020) and Guilmette et al. (2018). Data are from the following samples: a, 171212J01 (Wadi Tayin); b, 13OJGWT15 (Wadi Tayin); c, 171213J01 (Hammah Window); d, 171213J02 (Hammah Window); e, 171214J01 (Fanja; same outcrop as 181211M01); f, 171219J03 (Sumeini); g, 13OJGSW02 (Sumeini; same outcrop as 171219M06); h, 13OJGSW06 (Sumeini); i, 13OJGWT17 (Wadi Tayin; Garber et al., 2020); j, SU-03 (Sumeini), WT-150, WT-151 (Wadi Tayin; Guilmette et al., 2018). Samples 13OJGSW02 and 06 were collected from the same field stop as 13OJGSW01, but the samples were collected tens of metres apart. (b) Yb (ppm) versus Yb/Dy for all samples



## 5 | DISCUSSION

### 5.1 | Origin of zircon REE trends and the timing of sole metamorphism

Zircon trace element geochemistry—especially variations in the REE—can be used to link zircon crystallization to igneous or metamorphic phase assemblages. Variations in HREE concentrations and slope in zircon from garnet-bearing metamorphic rocks are typically attributed to partitioning of these elements between zircon and garnet (e.g., Kohn & Kelly, 2018; Rubatto, 2002; Rubatto & Hermann, 2007; Taylor et al., 2017, 2015). Partitioning data from both natural samples and experimental studies demonstrate that both zircon and garnet have a strong affinity for the HREE (Buick et al., 2006; Fornelli et al., 2014, 2018; Hermann & Rubatto, 2003; Hokada & Harley, 2004; Kelly & Harley, 2005; Kohn & Kelly, 2018; Rubatto, 2002; Rubatto & Hermann, 2003, 2007; Taylor et al., 2017, 2015; Whitehouse & Platt, 2003) and garnet growth prior to or synchronous with zircon leads to a depletion of zircon HREE. Several lines of evidence indicate that the observed variations in zircon HREE slopes in this study reflect *prograde* garnet growth:

1. Comparison of the zircon HREE data from garnet-free versus garnet-bearing amphibolites shows that the garnet-free amphibolites have  $\text{Yb/Dy} > 5$  and no trend in  $\text{Yb/Dy}$  versus  $\text{Yb}$ , whereas each garnet-bearing sample has a range in  $\text{Yb/Dy}$  from steep ( $\text{Yb/Dy} > 5$ ) to shallow ( $\text{Yb/Dy} < 5$ ) HREE slopes and the data define trends of decreasing  $\text{Yb/Dy}$  with decreasing  $\text{Yb}$  (Figures 3–5).
2. To understand the effect of all major phases on zircon REE, we analysed the main rock-forming minerals present in six garnet amphibolite samples and a subset of the minerals in two additional samples (Figure 7). In all of the analysed samples, garnet is the only phase with  $\text{Yb/Dy} > 1$  and is therefore the only major mineral that could lead to the observed decrease in zircon  $\text{Yb/Dy}$ ; REE sequestration in all other phases would lead to an increase in zircon  $\text{Yb/Dy}$ .
3. The combined zircon U–Pb and trace element data document a temporal evolution from older, high  $\text{Yb/Dy}$  to younger, low  $\text{Yb/Dy}$  zircon grains within individual samples, consistent with depletion of zircon HREE due to prograde garnet growth. In the Group A samples, single grain zircon dates show resolvable differences between high and low  $\text{Yb/Dy}$  grains in 9 out of the 12 samples, and the weighted mean date for high  $\text{Yb/Dy}$  zircon fractions is older than the weighted mean date for low  $\text{Yb/Dy}$  zircon fractions in all samples (Figure 5).

4. There is a correlation between increasing Ti-in-zircon temperature and decreasing  $\text{Yb/Dy}$  in many samples. We consider it most likely that the increase in Ti-in-zircon temperatures reflects a true increase in metamorphic temperature, although it could also reflect a decrease in  $a_{\text{SiO}_2}$  during prograde to peak partial melting (supporting information) (e.g., Guilmette et al., 2018; Soret et al., 2017). In either case, Ti-in-zircon versus  $\text{Yb/Dy}$  trends support prograde depletion of zircon HREE.
5. The temporal progression from high to low  $\text{Yb/Dy}$  zircon is texturally supported by grain-scale zircon core-rim relations in some samples (e.g., TA-16; Figures 2, S2 and S3). Likewise, synchronous zircon and garnet growth are texturally supported by the occurrence of zircon inclusions within garnet in the garnet amphibolites (Figures 8 and S9) (see also Soret et al., 2022); unfortunately, the imaged inclusions were too small for accurate and precise analysis by LA-ICP-MS or TIMS.
6. Estimated garnet-zircon HREE distribution coefficients from individual samples are broadly consistent with experimental values. Observed differences likely reflect analytical scatter, incomplete characterization of the chemistry of the different phases and/or differences between the metamorphic conditions in the sole and experiments, rather than indicating disequilibrium (supporting information; Figure S8).
7. The zircon trace-element trends are inconsistent with the observed trace element trends reflecting either partitioning with other accessory phases or zircon crystallization from a melt and strongly favour HREE partitioning between zircon and garnet (supporting information).
8. Other phases also show  $\text{Yb/Dy}$  changes that are consistent with the prograde influence of garnet. For example, Soret et al. (2022) similarly concluded that HREE depletions in titanite inclusions in garnet within garnet amphibolites from the Samail metamorphic sole reflect the progressive sequestration of HREE in prograde garnet.

For these reasons, we interpret the trend from older, high  $\text{Yb/Dy}$  ( $>5$ , blue data in Figure 5) to younger, low  $\text{Yb/Dy}$  ( $<5$ , red data in Figure 5) zircon in the garnet amphibolites as evidence for metamorphic zircon growth during or bracketing prograde garnet growth: High  $\text{Yb/Dy}$  zircon grew prior to or synchronously with early garnet, while low  $\text{Yb/Dy}$  zircon grew synchronously with low  $\text{Yb/Dy}$  garnet rims or after garnet growth. This prograde pattern is observed in 11 out of the 18 studied garnet amphibolites. A counter-clockwise pattern in  $\text{Yb/Dy}$  versus date in four Group B samples may reflect initial

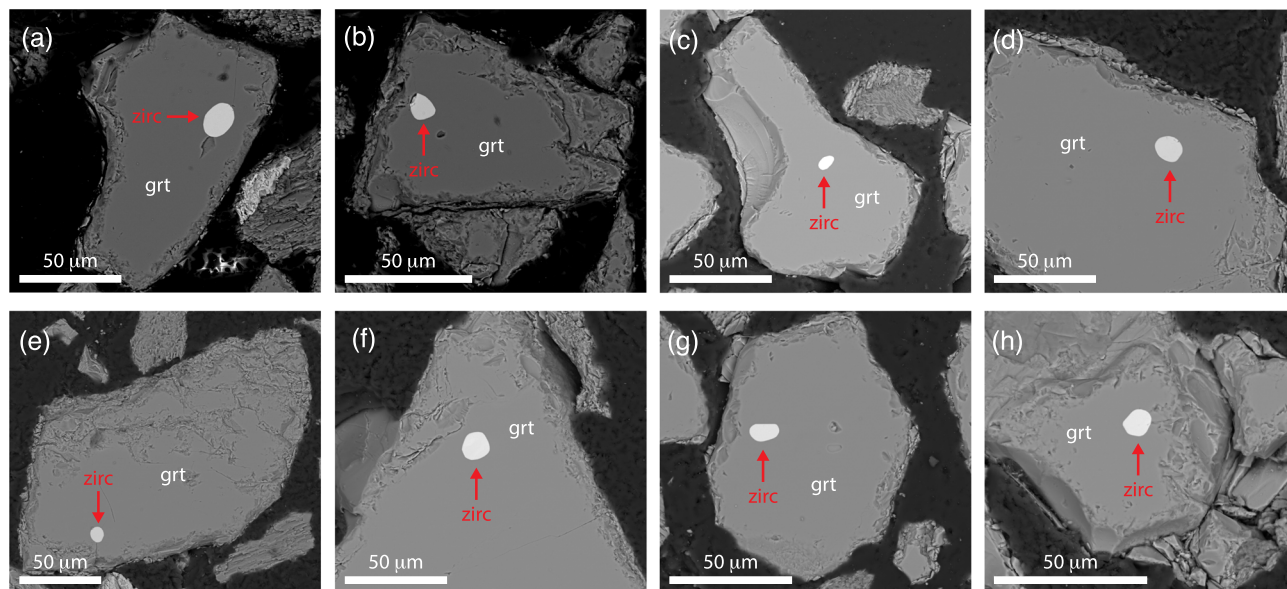


**FIGURE 8** Backscattered electron images of zircon inclusions within garnet in grain mounts from dated garnet amphibolite sample 171213J02. Each zircon inclusion was verified by energy dispersive spectroscopy. Additional inclusions are shown in Figure S9.

prograde garnet growth followed by the release of HREE during garnet break down on the retrograde path, which is supported by ongoing geochemical mapping of garnet. Overall, zircon data from 18 garnet amphibolite samples along the length of the ophiolite record prograde metamorphism between  $96.698 \pm 0.094$  and  $95.161 \pm 0.064$  Ma (based on the oldest and youngest precise dates— $2\sigma < 0.1$  Ma—from the garnet amphibolite samples).

The zircon forming reactions in these rocks were not directly constrained in this study; however, our analyses of the trace element chemistry of the major and accessory minerals provide some insight into the potential redistribution of Zr during prograde metamorphism. Mineral averages from eight garnet amphibolites (Table S4) indicate that amphibole (36–52 ppm), clinopyroxene (38–70 ppm) and garnet (7–26 ppm) contain tens of ppm of Zr, plagioclase contains negligible Zr and titanite contains hundreds of ppm of Zr (228–510 ppm). Zr concentrations in garnet are systematically lower than in clinopyroxene and amphibole, while amphibole and clinopyroxene from individual samples either have similar concentrations or clinopyroxene is enriched by  $\sim 20$  ppm. The mass balance of Zr during prograde metamorphism is dependent on the abundance of each phase, and the measured concentrations from the peak to retrograde amphibole in these samples may not be representative of lower temperature prograde amphibole; however, the fact that garnet is depleted in Zr relative to

amphibole, and the high Zr concentrations of the titanite show that amphibole and titanite breakdown could have driven prograde zircon growth.

## 5.2 | Hf isotope data and the protoliths of the metamorphic sole amphibolites

The zircon Hf data provide new insight into the protoliths of the sole samples. Previous isotopic data from the sole have been variable. Three sole amphibolites from Sumeini and Wadi Tayin yielded whole rock  $\varepsilon_{\text{Nd}}(t) = 3.9$ , 4.6 and 7.1 (Cox et al., 1999; Rioux et al., 2016) and a single garnet amphibolite sample from Masafi has zircon  $\varepsilon_{\text{Hf}}(t)$  of 5.6–10.0 (Kim et al., 2020). A metasediment and a leucocratic pod from Wadi Tayin yielded lower whole rock  $\varepsilon_{\text{Nd}}(t) = -7.0$  and  $-8.4$ , respectively (Garber et al., 2020; Rioux et al., 2013, 2016). The lower  $\varepsilon_{\text{Nd}}(t)$  for two of the three sole whole rock amphibolite samples raises the possibility that either the basaltic protoliths had low  $\varepsilon_{\text{Nd}}(t)$  or that some amphibolites include a meta-sedimentary component (Garber et al., 2020). Similarly, the negative  $\varepsilon_{\text{Nd}}(t)$  for a leucocratic pod from Wadi Tayin could indicate that some or all leucocratic pods in the sole reflect melting of sole metasediments, rather than amphibolites.

The zircon from the amphibolites and leucocratic pods analysed in this study generally yield high positive  $\varepsilon_{\text{Hf}}(t)$  values: zircon grains from 19 of the 22 analysed samples have weighted-mean  $\varepsilon_{\text{Hf}}(t)$  from +8.9 to +14.6,

and a single sample has a slightly lower weighted mean of +6.5. These values overlap but are generally slightly lower than whole rock lava  $\varepsilon_{\text{Hf}}(t)$  from the ophiolite crust (Figure 6 and Table S3): V1 and lower V2 lavas have  $\varepsilon_{\text{Hf}}(t) = 13.0$ –16.8, and upper V2 lavas have  $\varepsilon_{\text{Hf}}(t) = 12.2$ –14.2 (Kusano et al., 2017). The high  $\varepsilon_{\text{Hf}}(t)$  are consistent with the interpretation that the protolith to most sole amphibolites were oceanic basalts (Searle & Malpas, 1982), and the limited spread in  $\varepsilon_{\text{Hf}}(t)$  values suggest most amphibolites did not contain a significant sedimentary component prior to zircon growth, although the lower value for garnet-free amphibolite sample 171213M08 could reflect some sediment influence. The two studied leucocratic pods have  $\varepsilon_{\text{Hf}}(t)$  similar to the amphibolite compositions, consistent with the interpretation that they represent amphibolite partial melts (Cowan et al., 2014; Searle & Malpas, 1980).

Two of the analysed samples have more variable  $\varepsilon_{\text{Hf}}(t)$ . Sample 13OJGWT15 yielded zircon  $\varepsilon_{\text{Hf}}(t) = 4.5 \pm 2.7$  to  $12.5 \pm 2.8$  (MSWD = 3.3; Figure 6), potentially reflecting the impact of a metasedimentary component. The  $\varepsilon_{\text{Hf}}$  values are weakly correlated with Yb/Dy, with low Yb/Dy zircon having lower  $\varepsilon_{\text{Hf}}$ . Interestingly, the U–Pb and Yb versus Yb/Dy patterns are also distinct for this sample, with discrete dates for the high and low Yb/Dy populations—rather than the spread of U–Pb dates seen in other samples—and more consistent Yb concentrations over the range of Yb/Dy. The U–Pb, Yb/Dy and  $\varepsilon_{\text{Hf}}$  data are thus all consistent with distinct sources for the high Yb/Dy and low Yb/Dy zircon in this sample, perhaps reflecting fluxing by metasedimentary fluids or melts during zircon growth. The low Yb/Dy data are still offset to higher Ti-in-zircon temperatures, suggesting the data still reflect prograde metamorphism, although the differences in apparent temperature could also reflect different  $a_{\text{SiO}_2}$  or  $a_{\text{TiO}_2}$  activities.

Sample 181212M10 exhibits even more extreme variation, with  $\varepsilon_{\text{Hf}}(t) = -32.7 \pm 2.7$  to  $13.3 \pm 2.7$ . As discussed in the results (Section 4.5), grains with  $\varepsilon_{\text{Hf}}(t) = -18.1$  to  $-9.7$  have older U–Pb dates of 1,590–447 Ma (Table S1), with lower  $\varepsilon_{\text{Hf}}(t)$  corresponding to older dates. In contrast, zircon with U–Pb dates of  $\sim 96$  Ma within the sample define a single population of Hf data with a weighted mean  $\varepsilon_{\text{Hf}}(t) = 11.74 \pm 0.85$  ( $n = 10$ ; MSWD = 1.4). Given the two distinct populations—a  $\sim 96$  Ma population with  $\varepsilon_{\text{Hf}}(t) = 11.7$  and a 1590–447 Ma population with  $\varepsilon_{\text{Hf}}(t) = -18.1$  to  $-9.7$ —we consider it likely that the sample is a physical mixture, where the high  $\varepsilon_{\text{Hf}}(t)$  zircon grains come from metabasalt layers and the  $\varepsilon_{\text{Hf}}(t) < 0$  grains come from metasedimentary layers or melts. This interpretation is consistent with layering between amphibolite and extremely garnet-rich felsic bands at the outcrop scale.

### 5.3 | The spatial and temporal progression of sole metamorphism

Our new U–Pb dataset constrains the timing and duration of sole metamorphism along the length of the ophiolite. We will first discuss the garnet amphibolite dates, which zircon geochemistry indicates record or bracket the timing of prograde metamorphism (Sections 5.1), and then compare the timing of garnet-free amphibolite metamorphism and crystallization of leucocratic pods to the prograde garnet amphibolite dates. The broader implications of the spatial and temporal patterns described in this section are discussed in detail in Section 5.5. For the garnet amphibolite samples, we use the timing of the observed change from Yb/Dy > 5 to Yb/Dy < 5 zircon at each locality as a clear proxy for prograde garnet growth (the interpretations are similar if we instead compare the oldest zircon U–Pb date at each outcrop but would shift the dates back  $\sim 0.1$ –0.3 Myr).

In our previous work on the metamorphic sole of the Samail ophiolite, leucocratic pods from Sumeini and Wadi Tayin exposures recorded disparate dates of 96.2 and 94.8 Ma, respectively, suggesting a temporal gradient from northwest to southeast (Rioux et al., 2016). A similar spatial pattern still exists in the timing of prograde metamorphism, although the magnitude and absolute timing of the temporal gradient are different. Three garnet amphibolites from Sumeini record prograde dates of  $\sim 96.6$  Ma (Figure 9). In contrast, three garnet amphibolites from Wadi Tayin and Hammah in the southeast record younger dates of  $\sim 96.0$ –95.7 Ma, suggesting a  $\sim 0.6$  Myr offset between the onset of prograde garnet growth at Sumeini versus the southern sole localities. Garnet amphibolite data from the geographically intermediate localities of Fanja and Al Ajaiz yield intermediate dates (Figure 9), permissive of a smooth, relatively continuous temporal gradient from north to south (albeit with some complexity); however, more data are needed to critically evaluate this trend.

In the northernmost portion of the ophiolite—exposed in the UAE—the timing of the onset of prograde garnet growth ranges from  $\sim 96.4$  Ma (181219M03) to  $\sim 95.4$  Ma (181221M04) (Figure 9). The oldest dates from the Masafi exposure ( $\sim 96.6$  to 96.4 Ma) match the older ages for prograde garnet growth at the adjacent Sumeini locality; however, the dated samples from Masafi suggest a more prolonged metamorphic history at Masafi versus Sumeini, with the onset of prograde metamorphism lasting until  $\sim 95.4$  Ma (181220M07 and 181221M04; Figure 9). The youngest dates from Masafi are similar to or slightly younger than the garnet-amphibolite zircon U–Pb dates from southern parts of the ophiolite (Wadi Tayin and Fanja).

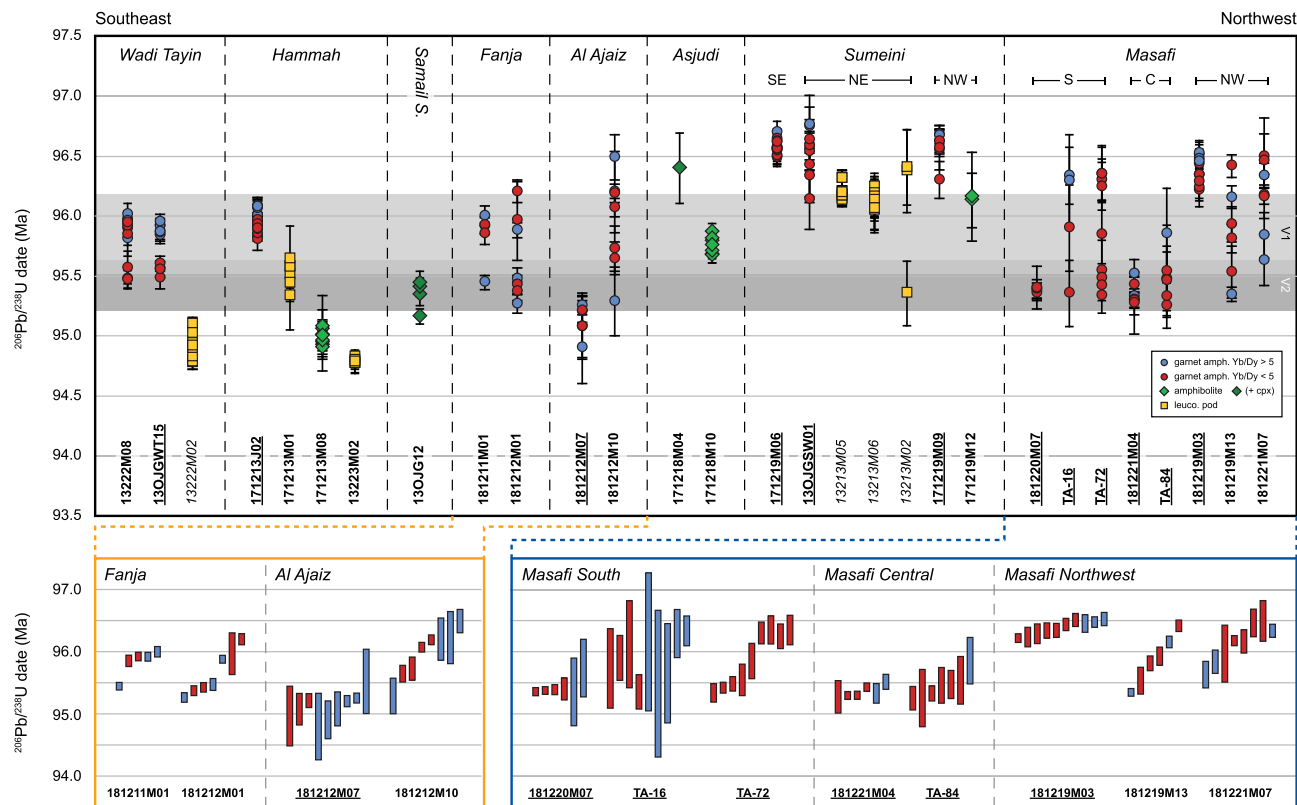


**FIGURE 9** Summary of the U–Pb dates from the metamorphic sole from this study (bold) and Rioux et al. (2016) (italics). Only data with  $\pm 2\sigma < 0.4$  Ma were included for samples from this study, for clarity—for the 2016 data, we plotted the same data as plotted in the original manuscript. The grey band shows the range of dates from V1 and V2 plutonic rocks in the ophiolite crust, based on interpreted crystallization ages, as outlined in Rioux, Garber, et al. (2021). Underlined sample numbers denote Group A samples (Figure 5). Data from Fanja, Al Ajaiz and Masafi are shown in detail below. Garnet amphibolites are plotted in blue and red, and garnet-free amphibolites are in green.

Combined with our previous results (Rioux et al., 2016), our new data also show that there is an offset between the timing of zircon crystallization and garnet growth in garnet amphibolites versus the timing of zircon crystallization in the structurally lower garnet-free amphibolites and leucocratic pods at each sole locality (Figure 9). At Sumeini, the onset of prograde zircon crystallization in garnet amphibolites was at  $\sim 96.7$  Ma (based on the oldest zircon dates), whereas one garnet-free amphibolite and two leucocratic pods (excluding texturally late vein sample 13213M02) yield dates of  $\sim 96.15$ , indicating an offset of  $\sim 0.5$  Ma. The youngest zircon from the HTa amphibolites overlap the zircon dates from the HTb samples, permitting overlap between the end of the high-grade metamorphism in the garnet amphibolites and prograde to peak metamorphism in the lower temperature garnet-free amphibolites. Garnet amphibolites from Wadi Tayin and Hammah Window record the onset of prograde zircon growth from 96.1–96.0 Ma, while a garnet-free amphibolite and two leucocratic pods yield dates of  $\sim 95.0$ – $94.8$  Ma, suggesting an offset in the

initiation of garnet amphibolite versus garnet-free amphibolite metamorphism of 1.0–1.3 Myr. The offset between the youngest high-grade zircon grains and the oldest lower grade zircon grains at these localities suggest that the high-grade metamorphism of the garnet amphibolites (HTa) ceased 0.4 Myr before growth in the lower grade garnet-free amphibolites. A single leucocratic vein that is parallel to foliation in Hammah has an earlier date of  $\sim 95.5$  Ma (171213M01), which may reflect retrograde melting of HTa amphibolites during exhumation prior to lower grade HTb metamorphism. This interpretation is supported by higher Ti-in-zircon temperatures in this sample (602–782°C, average = 709°C) compared to the other leucocratic pod from Hammah (13223M02; 604–740°C, average = 667°C; Figure 4). There is also an offset between the higher grade clinopyroxene-bearing amphibolite ( $96.32 \pm 0.25$  Ma) and the clinopyroxene-free amphibolite ( $\sim 95.87$ – $95.67$  Ma) from Asjudi.

A final garnet-free amphibolite sample from Samail South (130JG12) has textures that are ambiguous regarding the peak metamorphic conditions, that is, whether or



not it was once a higher grade, garnet-bearing sample. The sample contains abundant clinopyroxene but comes from a small outcrop without a clear geologic context, and the dates from the sample are similar to the garnet-free amphibolites from the other sole exposures in the southern massifs. This sample is interesting because it comes from the leading edge of the ophiolite, like the Sumeini and Masafi exposures, whereas the other sole localities from the southern massifs are from the trailing edge. While the context of the sample is poorly constrained, the younger date matches the dates from similar Wadi Tayin and Hammah sole rocks and suggests that the age offset between the northern versus southern massifs reflects a northwest to southeast age progression, rather than a temporal difference between the leading versus trailing edge of the ophiolite.

There is broad agreement between the zircon crystallization ages of the youngest leucocratic pods and garnet-free amphibolites at each locality:  $\sim 95.0$ – $94.8$  Ma at Wadi Tayin/Hammah and  $\sim 96.15$  Ma at Sumeini. We therefore attribute the pods to melting of the lower grade (HTb) amphibolites and interpret the zircon dates from the pods and garnet-free amphibolites to record the timing of the lower grade (HTb) metamorphism—with the possible exception of the older leucocratic vein sample 171213M01 from Hammah. The zircon chemistry from the garnet-free amphibolites does not constrain whether the zircon grew on the prograde or retrograde path; however, interpreted peak  $P$ – $T$  conditions for the lower grade amphibolites were near the solidus (e.g., Soret et al., 2017), so the agreement between the dates of the leucocratic pods and garnet-free amphibolites suggest the dates record the timing of near-peak conditions.

The duration of metamorphic zircon dates within each sample constrains the minimum duration of high-grade metamorphic conditions during garnet growth ( $\sim 650$ – $800^\circ\text{C}$ ). For the garnet amphibolites, most samples with precise data suggest a minimum duration of metamorphism from  $\sim 200$ – $600$  kyr, with four samples potentially showing a longer duration of up to  $\sim 1$  Myr (supporting information). The U–Pb systematics for the four samples that record a longer duration are complex and the range of zircon dates in these samples may not simply reflect metamorphic zircon growth.

## 5.4 | Implications for subduction initiation

As outlined in the introduction, the timing of sole metamorphism relative to formation of the ophiolite crust is crucial for understanding the geodynamic processes of subduction initiation (Guilmette et al., 2018): Early

thrusting during induced subduction initiation may lead to sole metamorphism millions of years prior to ophiolite formation (e.g., Gurnis et al., 2004; Leng et al., 2012), whereas spontaneous initiation will lead to near-synchronous sole metamorphism and ophiolite magmatism (e.g., Maunder et al., 2020; Stern & Bloomer, 1992).

The data presented here—particularly the interplay between zircon U–Pb dates, HREE concentrations, Ti-in-zircon temperatures and the textural evidence for zircon inclusions in garnet—directly link metamorphic zircon dates to garnet growth and definitively show that prograde ( $\sim 650$ – $800^\circ\text{C}$ ) metamorphic sole garnet growth occurred between  $96.698 \pm 0.094$  and  $95.161 \pm 0.064$  Ma along the length of the Samail ophiolite, with the duration of metamorphism spanning only a portion of this range ( $\sim 100$ s ka) at each location. The high Yb/Dy of the oldest zircon from the garnet amphibolites—which are similar to garnet-free samples from this study—argues strongly against the presence of a significant volume of garnet prior to zircon growth.

The zircon data are therefore inconsistent with previously reported 104–103 Ma garnet amphibolite Lu–Hf dates (Guilmette et al., 2018) and suggest that the Lu–Hf isochron dates do not accurately record the timing of garnet growth in the Samail metamorphic sole. We cannot say definitively why the Lu–Hf results are inaccurate; however, we note that the Lu–Hf isochrons from the Guilmette et al. (2018) study yield low initial  $\varepsilon_{\text{Hf}}$  of  $-5$  to  $-12$ . These values are much lower than our reproducible zircon  $\varepsilon_{\text{Hf}}$  values of  $+6.5$  to  $+14.6$  from garnet amphibolites from the same (and numerous other) outcrops, which presumably reflect the isotopic composition of the protolith (Figure 6).

Soret et al. (2022) also recently reported LA-ICP-MS titanite dates from garnet amphibolites in the sole, with apparently intermediate dates of  $100 \pm 2$  to  $94.7 \pm 0.8$  Ma, suggesting prolonged sole metamorphism. However, the calculated dates from Soret et al. (2022) are dependent on the assumed common Pb composition, because all of the spot data are discordant and plot along common-Pb tie lines. The published dates were calculated assuming a set common-Pb isotopic composition based on the Stacey and Kramers (1975) model ( $^{207}\text{Pb}/^{206}\text{Pb} = 0.84$ ), but unanchored regressions of the same data suggest variable common Pb composition with  $^{207}\text{Pb}/^{206}\text{Pb}$  that are often lower than the Stacey and Kramers (1975) model. Lower intercept dates for the unanchored regressions range from  $98.6 \pm 5.3$  to  $93.8 \pm 3.3$  Ma (excluding a single younger date with large uncertainties), with most dates ranging from 97 to 94 Ma (calculated in IsoplotR using unanchored Model 1 discordia) (Vermeesch, 2018). All of the recalculated dates overlap the range in zircon dates from the garnet amphibolite

samples reported herein, within uncertainty. In the published dates reduced using a fixed common Pb composition, five titanite populations with distinct trace element chemistry from a single sample (SE14-31) yielded a range in dates of  $\sim 5$  Ma; however, the same five populations all yield the same date within uncertainty ( $\sim 95$  Ma) when the data are regressed without an assumed common Pb composition, arguing against prolonged titanite growth. Monazite data from the same study also yield ambiguous results: The Soret et al. (2022) data define two populations based on trace element geochemistry, which yield  $^{208}\text{Pb}/^{232}\text{Th}$  weighted mean dates of  $98.9 \pm 0.5$  and  $97.9 \pm 0.8$  Ma, but both have younger  $^{206}\text{Pb}/^{238}\text{U}$  weighted mean dates of  $95.5 \pm 0.4$  and  $95.0 \pm 0.7$  Ma. The  $^{206}\text{Pb}/^{238}\text{U}$  dates again overlap our zircon U–Pb dates from the sole, and—because monazite U–Th–Pb standards often have a calculated or assumed  $^{208}\text{Pb}/^{232}\text{Th}$  value, rather than a measured one—it is not possible to determine whether the  $^{208}\text{Pb}/^{232}\text{Th}$  or  $^{206}\text{Pb}/^{238}\text{U}$  dates are ‘correct’. Overall, the Soret et al. (2022) data are sensitive to the chosen reduction parameters, and when reduced differently, the data are entirely consistent with the new U–Pb zircon dates from our study.

Our new zircon U–Pb dates from the metamorphic sole (96.7–95.2 Ma) demonstrate that the earliest high-grade metamorphism predated initial magmatism within the ophiolite by  $\sim 600$  ka but continued throughout ophiolite growth (96.1–95.2 Ma; Figure 9). This smaller sole-ophiolite offset is consistent with ophiolite formation through spontaneous subduction initiation (e.g., Maunder et al., 2020)—as has been inferred for the IBM system (Arculus et al., 2015; Maunder et al., 2020; Stern & Bloomer, 1992; Stern & Gerya, 2018)—or a much shorter duration of pre-subduction thrusting during induced subduction initiation. While we cannot discount the possibility that there was earlier thrusting related to induced subduction initiation, evidence of any earlier deformation is not preserved in the ophiolite or sole. Given the constraints of the rock record, the offset between the onset of prograde sole metamorphism and ophiolite magmatism records a minimum duration for initiation and nascent subduction of  $\sim 600$  ka prior to ophiolite formation. Together, the sole and ophiolite preserve a record of the first  $\sim 1.5$  Ma of subduction—the span of dates in the metamorphic sole and overlying ophiolite crust.

## 5.5 | The tectonic development of the metamorphic sole

The combined record of ophiolite magmatism and sole metamorphism provide new insight into the tectonic development of the ophiolite. The new data presented

here record a shift in the timing of initial prograde metamorphism observed in the highest grade garnet amphibolite samples from Masafi/Sumeini ( $\sim 96.6$  Ma) to Wadi Tayin/Hammah ( $\sim 96.0$ – $95.7$  Ma), which is mirrored in dates from the lower grade amphibolites and leucocratic pods from the same localities ( $\sim 96.2$  to  $94.8$  Ma) (Rioux et al., 2016). In addition, we have shown in our previous work that later felsic intrusions into the ophiolite mantle and crust—which have low  $\epsilon_{\text{Nd}}$  and  $\epsilon_{\text{Hf}}$  and elevated  $\delta^{18}\text{O}$  and have previously been attributed to melting of amphibolite and sediment on the subducting slab (Amri et al., 2007; Haase et al., 2015; Rioux, Benoit, et al., 2021; Rollinson, 2014, 2015; Spencer et al., 2017)—display a significant variation from south to north, with dates of  $95.2$ – $95.0$  Ma in the Oman portion of the ophiolite compared to younger dates of  $94.1$ – $91.0$  Ma in the UAE section (Rioux, Garber, et al., 2021).

The tectonic implications of the timing of prograde metamorphism in the highest grade garnet amphibolites are dependent on the specific processes of sole accretion, which are not definitively known. Here, we discuss the new data for the highest grade rocks in the context of two potential models for sole accretion, before then considering the offset between the garnet amphibolite and garnet-free amphibolite dates:

### 1. Model 1, Rheological controls on sole accretion:

Several studies have suggested that accretion of the sole is linked to rheological coupling between the sole and overlying mantle at the subduction interface, due to either strengthening of the mantle and thermal weakening of the slab (Agard et al., 2020, 2016; Hacker, 1990, 1991) or strengthening of the slab relative to the mantle due to metamorphic phases changes (Ambrose et al., 2021). In these models, the rheological transitions are linked to changes in  $P$ – $T$  conditions related to the transient thermal structure of the subduction interface during subduction initiation or initial thrusting below the ophiolite. The detachment of the high-temperature soles may be a discrete event in the thermal evolution of the nascent subduction zone or represent multiple discrete detachment events that each occurred over a longer but finite window of time ( $\sim 1$  Ma) (Soret et al., 2017). In the context of these models, the highest grade rocks in each sole locality would reflect the timing when the nascent slab first reached  $\sim 800^\circ\text{C}$  (the proposed temperature of rheological coupling). The progression of prograde dates from Sumeini to Wadi Tayin would then indicate that subduction started in the northwest and propagated to the southeast (present geographical reference frame; Figure 10a). The  $0.6$  Myr offset would suggest propagation rates of  $\sim 540$  km/Ma, which—while faster

than many plate tectonic rates—are consistent with geochronology that suggests near synchronous initiation along the entire 1,700 km length of the IBM forearc (Reagan et al., 2019). In this model, the younger felsic mantle dikes in the UAE may reflect subduction of a thick section of continental detritus or the continental margin below the northernmost portion of the ophiolite soon after ophiolite formation, due to the preexisting shape of the margin. The consistent ages of V1 and V2 magmatism along the length of the ophiolite indicate that if the metamorphic dates from the sole do reflect southward propagation of the subduction zone, this was not reflected in the timing of initial magmatism in the overlying ophiolite.

2. **Model 2, Slab rotation:** Alternately, the progression of ages from Sumeini to Wadi Tayin could reflect variable subduction rates along the length of the ophiolite, with faster subduction in the southeast (Rioux et al., 2016) (present geographical reference frame; Figure 10b). Placing the new sole dates in the context of this model, our new U–Pb zircon dates would require that subduction initiated prior to ~96.8 Ma. The Sumeini and Masafi sole localities then reached depths of ~1 GPa at ~96.6 Ma but stalled at that depth. Faster subduction continued in the southeast until the rocks from Wadi Tayin and Hammah underwent metamorphism at ~96.0 Ma. The entire HTa sole may have then been welded to the overlying

mantle and exhumed as single slab. In this model, the Euler pole of rotation would be located close to the northern end of the ophiolite, which has been independently suggested based on paleomagnetic data (Morris et al., 2016; van Hinsbergen et al., 2019). The slower subduction—and therefore slower cooling—in the north is consistent with the intrusion of younger felsic mantle dikes and the high temperatures (770–900°C) of the younger (94.5–92.6 Ma) out-of-sequence Bani Hamid thrust sheet (Searle et al., 2015). The prolonged period of zircon growth at the Masafi sole locality (Figure 9) may also reflect a longer high-temperature history, although some of the variability in dates is likely also linked to variations in the protolith compositions. In this model, it may be that the rheological coupling proposed by Agard et al. (2020, 2016) and Ambrose et al. (2021) is the physical process by which the high-grade metamorphic soles are detached from the downgoing slab but that the ultimate preservation and juxtaposition of the sole with the base of the ophiolite are dictated by larger scale tectonic considerations. The ~96.0 Ma age of the youngest high-grade sole metamorphism at Wadi Tayin and Hammah localities corresponds to the initiation of magmatism within the ophiolite (Rioux et al., 2012, 2013, 2016; Rioux, Garber, et al., 2021), and perhaps, the preservation of the sole is linked to the beginning of slab rollback and extension in the overriding plate.

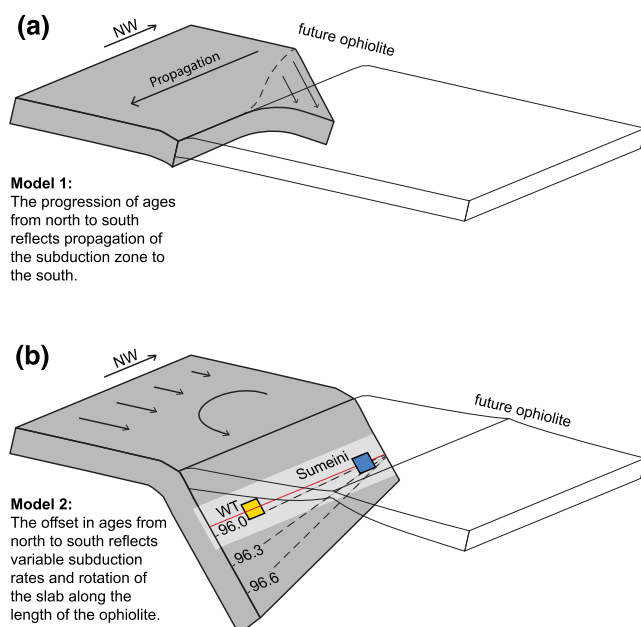


**FIGURE 10** Tectonic models to explain the progression of ages between the northern and southern sole localities. WT, Wadi Tayin. Model 2 is after Rioux et al. (2016).

The offset between the timing of zircon growth in the garnet amphibolites and garnet-free amphibolite-leucocratic pods along the length of the ophiolite provides further insight into the development of subduction (Section 5.3). This offset ranges from ~0.5 Myr at Sumeini to 1.0–1.3 Myr at Wadi Tayin/Hammah. In general, the observed offset in zircon U–Pb dates between garnet amphibolites and the lower grade garnet-free amphibolites indicates that in addition to the inverted thermal gradient in the sole, there is also a temporal gradient from older, high-grade rocks at the top (HTa) to younger, lower grade rocks below (HTb) (Garber et al., 2020). As a result, the different thrust sheets of the sole do not represent a contemporaneous snapshot of temperatures along the subduction interface but instead reflect a continually evolving thermal structure of the nascent subduction zone.

The implications of the offset between the timing of higher grade and lower grade amphibolites again depend on the mechanisms of sole formation. Thermobarometry from the sole suggests there is an offset in peak pressures and temperatures between these units; Cowan et al. (2014) reported peak *P–T* conditions of 1.1–1.3 GPa, 770–900°C (HTa) versus 0.9 GPa, 700–750°C (HTb), and Soret

et al. (2017) inferred a similar offset with  $P$ - $T$  of 0.8–1.0 GPa, 800–900°C (HTa) versus 0.7–0.9 GPa, 675–775°C (HTb). Assuming that the garnet-free amphibolites reached peak conditions prior to or synchronously with their structural juxtaposition with the higher grade garnet amphibolites and that the U–Pb dates record the timing of near-peak conditions, the offset in the U–Pb dates between higher and lower grade amphibolites would suggest that detachment and ~0.1–0.2 GPa of exhumation of the garnet amphibolites occurred over 0.5–1.3 Myr. In this model, it is not clear why the zircon age offset between the garnet-bearing and garnet-free samples increases from Sumeini to Wadi Tayin, although if subduction was faster in the southern portion of the ophiolite (Model 2), perhaps the slower exhumation rate of the highest grade rocks is related to the increased subduction rate, providing a stronger downgoing basal traction and inhibiting movement of material back up the subduction channel.

Alternately, Ambrose et al. (2021) argued the garnet amphibolites (HTa) and garnet-free amphibolites (HTb) formed at similar pressures. These authors found consistent pressures of 1.0–1.2 GPa from both garnet amphibolites and garnet-free epidote amphibolites from a 250 m thick sole at Masafi, with a gradient in peak temperatures from ~800–900°C to ~650°C. They concluded that the apparent offset in pressures between HTa and HTb units in Soret et al. (2017) may be an artefact of phase equilibrium  $P$ - $T$  modelling and the choice of their equilibrium metamorphic assemblage; further, though Soret et al. (2017) argue for a ~0.2 GPa pressure offset between their HTa and HTb units, their reported pressures from these units overlap within uncertainty. These data raise the possibility that the highest grade garnet amphibolites and lower grade garnet-free amphibolites formed at the same depth, but at different temperatures and times, as the subduction zone evolved: The garnet amphibolites formed first at ~800°C and 1 GPa, before being detached from the descending slab, then continued subduction below these rocks led to metamorphism of the garnet-free amphibolites at the same depths (~1 GPa), but lower temperatures (~650–750°C) as the subduction interface progressively cooled. This model naturally juxtaposes the lower grade amphibolites (HTb) with the base of the higher grade unit (HTa), before detachment and exhumation of the combined HTa-HTb package. In this model, the offset in dates between the higher and lower grade amphibolites would reflect the rate of subduction, and the difference in this offset between Sumeini (0.5 Ma) and Wadi Tayin/Hammah (1.0–1.3 Ma) would suggest *slower* subduction in the south—in conflict with Model 2 above. If the high  $P$  estimates for the low temperature sole from Kotowski

et al. (2021) are accurate, the low temperature sole may have also been subducted to ~1 GPa and juxtaposed with the HT sole at these depths. In either of the models outlined above, the hornblende  $^{40}\text{Ar}/^{39}\text{Ar}$  cooling dates from the sole ( $95.7 \pm 0.6$  to  $92.6 \pm 1.2$  Ma) suggest rapid cooling of the sole following peak metamorphism (Hacker et al., 1996).

## 6 | CONCLUSIONS

- New coupled zircon trace element analyses and high-precision U–Pb dating directly constrain the timing of prograde- to peak-metamorphism in the metamorphic sole of the Samail ophiolite.
- Trends of decreasing Yb/Dy with decreasing Yb in zircon from garnet amphibolites record progressive depletion of the HREE during prograde-to-peak garnet growth. High precision dates from these samples indicate that prograde garnet and zircon growth in the highest grade rocks occurred between  $96.698 \pm 0.094$  and  $95.161 \pm 0.064$  Ma.
- The prograde to peak U–Pb dates are significantly younger than recently reported Lu–Hf dates of ~104–103 Ma ( $n = 3$ ) from two of the same sole localities (Guilmette et al., 2018) and suggest that the Lu–Hf isochrons do not accurately reflect the timing of prograde metamorphism.
- The new data record a gradient in the timing of prograde to peak metamorphism from the northern (Sumeini/Masafi; ~96.7–96.3 Ma) to southern massifs (Wadi Tayin/Hammah; ~96.0–95.5 Ma), likely recording either propagation of the nascent subduction zone or changes in the rate of subduction along the length of the ophiolite.
- Prograde to peak metamorphism in the sole (96.7–95.2 Ma) began ~0.6 Myr prior to and then overlapped the timing of ophiolite magmatism (96.1–95.2 Ma), consistent with either spontaneous subduction initiation or an abbreviated period of initial thrusting (~0.6 Ma) during induced subduction initiation.
- The new U–Pb data provide a precise temporal record of subduction initiation in the Samail ophiolite and can be used to calibrate and test both numerical and geologic models of this important—but still incompletely understood—process.

## ACKNOWLEDGEMENTS


This research was supported by the United States National Science Foundation grants EAR-1650407 and 1250522 to Matthew Rioux and EAR-2120931 to Joshua Garber. We thank the Public Authority for Mining for



their support of our research in the Sultanate of Oman and Mohammed Ali and Aisha Al Suwaidi at Khalifa University for all their help during our field work in the United Arab Emirates. We are grateful for the assistance of Nasser AL Rizeiqi from the Public Authority for Mining during field work in Oman. We thank Alexandra Nicklin for her assistance in the field and her work on a subset of the UAE samples. We thank Gareth Seward for maintaining and helping run the SEM and EPMA at UCSB and Julia Dennis for digitizing spot locations on the cathodoluminescence images (Figure S1). Yann Rolland, Chris Yakymchuk, Alissa Kotowski, Michael Eddy, one anonymous reviewer and Editor Johann Diener provided valuable feedback that significantly improved the manuscript.

## ORCID

Matthew Rioux  <https://orcid.org/0000-0003-4765-6982>

Joshua M. Garber  <https://orcid.org/0000-0001-5313-0982>

Michael Searle  <https://orcid.org/0000-0001-6904-6398>

Sally Stevens  <https://orcid.org/0000-0002-0874-9636>

Andrew Kylander-Clark  <https://orcid.org/0000-0002-4034-644X>

Tyler Ambrose  <https://orcid.org/0000-0001-8971-8446>

## REFERENCES

- Agard, P., Jolivet, L., Vrielynck, B., Burov, E., & Monié, P. (2007). Plate acceleration: The obduction trigger? *Earth and Planetary Science Letters*, 258, 428–441. <https://doi.org/10.1016/j.epsl.2007.04.002>
- Agard, P., Prigent, C., Soret, M., Dubacq, B., Guillot, S., & Deldicque, D. (2020). Slabification: Mechanisms controlling subduction development and viscous coupling. *Earth-Science Reviews*, 208, 103259. <https://doi.org/10.1016/j.earscirev.2020.103259>
- Agard, P., Yamato, P., Soret, M., Prigent, C., Guillot, S., Plunder, A., Dubacq, B., Chauvet, A., & Monié, P. (2016). Plate interface rheological switches during subduction infancy: Control on slab penetration and metamorphic sole formation. *Earth and Planetary Science Letters*, 451, 208–220. <https://doi.org/10.1016/j.epsl.2016.06.054>
- Alabaster, T., Pearce, J. A., & Malpas, J. (1982). The volcanic stratigraphy and petrogenesis of the Oman ophiolite complex. *Contributions to Mineralogy and Petrology*, 81, 168–183. <https://doi.org/10.1007/BF00371294>
- Ambrose, T. K., Wallis, D., Hansen, L. N., Waters, D. J., & Searle, M. P. (2018). Controls on the rheological properties of peridotite at a palaeosubduction interface: A transect across the base of the Oman–UAE ophiolite. *Earth and Planetary Science Letters*, 491, 193–206. <https://doi.org/10.1016/j.epsl.2018.03.027>
- Ambrose, T. K., Waters, D. J., Searle, M. P., Gopon, P., & Forshaw, J. B. (2021). Burial, accretion, and exhumation of the metamorphic sole of the Oman–UAE ophiolite. *Tectonics*, 40, e2020TC006392.
- Amri, I., Ceuleneer, G., Benoit, M., Python, M., Puga, E., & Targuisti, K. (2007). Genesis of granitoids by interaction between mantle peridotites and hydrothermal fluids in oceanic spreading setting in the Oman ophiolite. *Geogaceta*, 42, 23–26.
- Arculus, R. J., Ishizuka, O., Bogus, K. A., Gurnis, M., Hickey-Vargas, R., Aljahdali, M. H., Bandini-Maeder, A. N., Barth, A. P., Brandl, P. A., Drab, L., do Monte Guerra, R., Hamada, M., Jiang, F., Kanayama, K., Kender, S., Kusano, Y., Li, H., Loudin, L. C., Maffione, M., ... Zhang, Z. (2015). A record of spontaneous subduction initiation in the Izu–Bonin–Mariana arc. *Nature Geoscience*, 8, 728–733. <https://doi.org/10.1038/ngeo2515>
- Bailey, E. H. (1981). Geologic map of Muscat-Ibra area, Sultanate of Oman. *Journal of Geophysical Research*, 86, map.
- Belgrano, T. M., & Diamond, L. W. (2019). Subduction-zone contributions to axial volcanism in the Oman–U.A.E. ophiolite. *Lithosphere*, 11, 399–411. <https://doi.org/10.1130/L1045.1>
- Belgrano, T. M., Diamond, L. W., Vogt, Y., Biedermann, A. R., Gilgen, S. A., & Al-Tobi, K. (2019). A revised map of volcanic units in the Oman ophiolite: Insights into the architecture of an oceanic proto-arc volcanic sequence. *Solid Earth*, 10, 1181–1217. <https://doi.org/10.5194/se-10-1181-2019>
- Boudier, F., Ceuleneer, G., & Nicolas, A. (1988). Shear zones, thrusts and related magmatism in the Oman ophiolite: Initiation of thrusting on an oceanic ridge. *Tectonophysics*, 151, 275–296. [https://doi.org/10.1016/0040-1951\(88\)90249-1](https://doi.org/10.1016/0040-1951(88)90249-1)
- Boudier, F., Nicolas, A., & Ildefonse, B. (1996). Magma chambers in the Oman ophiolite: Fed from the top and the bottom. *Earth and Planetary Science Letters*, 144, 239–250. [https://doi.org/10.1016/0012-821X\(96\)00167-7](https://doi.org/10.1016/0012-821X(96)00167-7)
- Bowring, J. F., McLean, N. M., & Bowring, S. A. (2011). Engineering cyber infrastructure for U–Pb geochronology: Tripoli and U–Pb\_Redux. *Geochemistry, Geophysics, Geosystems*, 12, Q0AA19. <https://doi.org/10.1029/2010GC003479>
- Buick, I. S., Hermann, J., Williams, I. S., Gibson, R. L., & Rubatto, D. (2006). A SHRIMP U–Pb and LA–ICP–MS trace element study of the petrogenesis of garnet–cordierite–orthoamphibole gneisses from the Central Zone of the Limpopo Belt, South Africa. *Lithos*, 88, 150–172. <https://doi.org/10.1016/j.lithos.2005.09.001>
- Cherniak, D. J., & Watson, E. B. (2001). Pb diffusion in zircon. *Chemical Geology*, 172, 5–24. [https://doi.org/10.1016/S0009-2541\(00\)00233-3](https://doi.org/10.1016/S0009-2541(00)00233-3)
- Cherniak, D. J., Watson, E. B., Grove, M., & Harrison, T. M. (2004). Pb diffusion in monazite: A combined RBS/SIMS study 1 Associate editor: Y. Amelin. *Geochimica et Cosmochimica Acta*, 68, 829–840. <https://doi.org/10.1016/j.gca.2003.07.012>
- Cowan, R. J., Searle, M. P., & Waters, D. J. (2014). Structure of the metamorphic sole to the Oman ophiolite, Sumeini window and Wadi Tayyin: Implications for ophiolite obduction processes. *Geological Society, London, Special Publications*, 392, 155–175. <https://doi.org/10.1144/SP392.8>
- Cox, J., Searle, M., & Pedersen, R. (1999). The petrogenesis of leucogranitic dykes intruding the northern Semail ophiolite, United Arab Emirates: Field relationships, geochemistry and Sr/Nd isotope systematics. *Contributions to Mineralogy and Petrology*, 137, 267–287. <https://doi.org/10.1007/s004100050550>
- Cox, J. S. (2000). *Subduction-obduction related petrogenetic and metamorphic evolution of the Semail ophiolite sole in Oman and the United Arab Emirates* (p. 175). University of Oxford.

- Crowley, J. L. (2018). Laser cutting of zircon for CA-TIMS geochronology: Adding spatial resolution to high-precision dates, GSA Annual Meeting in Indianapolis, Indiana, USA-2018. GSA.
- Ernewein, M., Pflumio, C., & Whitechurch, H. (1988). The death of an accretion zone as evidenced by the magmatic history of the Sumail ophiolite (Oman). *Tectonophysics*, 151, 247–274. [https://doi.org/10.1016/0040-1951\(88\)90248-X](https://doi.org/10.1016/0040-1951(88)90248-X)
- Ferry, J. M., & Watson, E. B. (2007). New thermodynamic models and revised calibrations for the Ti-in-zircon and Zr-in-rutile thermometers. *Contributions to Mineralogy and Petrology*, 154, 429–437. <https://doi.org/10.1007/s00410-007-0201-0>
- Fornelli, A., Langone, A., Micheletti, F., Pascazio, A., & Piccarreta, G. (2014). The role of trace element partitioning between garnet, zircon and orthopyroxene on the interpretation of zircon U–Pb ages: An example from high-grade basement in Calabria (Southern Italy). *International Journal of Earth Sciences*, 103, 487–507. <https://doi.org/10.1007/s00531-013-0971-8>
- Fornelli, A., Langone, A., Micheletti, F., & Piccarreta, G. (2018). REE partition among zircon, orthopyroxene, amphibole and garnet in a high-grade metabasic system. *Geological Magazine*, 155, 1705–1726. <https://doi.org/10.1017/S001675681700067X>
- Garber, J. M., Rioux, M., Kylander-Clark, A. R. C., Hacker, B. R., Vervoort, J. D., & Searle, M. P. (2020). Petrochronology of Wadi Tayin metamorphic sole metasediment, with implications for the thermal and tectonic evolution of the Samail ophiolite (Oman/UAE). *Tectonics*, 39, e2020TC006135. <https://doi.org/10.1029/2020TC006135>
- Gass, I. G., Bartholomew, I. D., Brown, M. A., Browning, P., Graham, G. M., Lippard, S. J., Robertson, A. H. F., Rothery, D. A., Searle, M. P., Smewing, J. D., & Woodcock, N. H. (1983). *Open University Oman ophiolite project (memoir map)*. The Open University.
- Gerya, T. (2011). *Intra-oceanic subduction zones, arc-continent collision* (pp. 23–51). Springer. [https://doi.org/10.1007/978-3-540-88558-0\\_2](https://doi.org/10.1007/978-3-540-88558-0_2)
- Gerya, T. V., Connolly, J. A., & Yuen, D. A. (2008). Why is terrestrial subduction one-sided? *Geology*, 36, 43–46. <https://doi.org/10.1130/G24060A.1>
- Ghent, E. D., & Stout, M. Z. (1981). Metamorphism at the base of the Samail ophiolite, Southeastern Oman Mountains. *Journal of Geophysical Research*, 86, 2557–2571. <https://doi.org/10.1029/JB086iB04p02557>
- Gnos, E. (1992). *The metamorphic rocks associated with the Semail ophiolite (Sultanate of Oman and United Arab Emirates)*. Bern University.
- Gnos, E. (1998). Peak metamorphic conditions of garnet amphibolites beneath the Semail ophiolite: Implications for an inverted pressure gradient. *International Geology Review*, 40, 281–304. <https://doi.org/10.1080/00206819809465210>
- Gnos, E., & Peters, T. (1993). K–Ar ages of the metamorphic sole of the Semail ophiolite: Implications for ophiolite cooling history. *Contributions to Mineralogy and Petrology*, 113, 325–332. <https://doi.org/10.1007/BF00286925>
- Godard, M., Bosch, D., & Einaudi, F. (2006). A MORB source for low-Ti magmatism in the Semail ophiolite. *Chemical Geology*, 234, 58–78. <https://doi.org/10.1016/j.chemgeo.2006.04.005>
- Godard, M., Dautria, J. M., & Perrin, M. (2003). Geochemical variability of the Oman ophiolite lavas: Relationship with spatial distribution and paleomagnetic directions. *Geochemistry, Geophysics, Geosystems*, 4, 8609. <https://doi.org/10.1029/2002GC000452>
- Goodenough, K., Styles, M., Schofield, D., Thomas, R., Crowley, Q., Lilly, R., McKerver, J., Stephenson, D., & Carney, J. (2010). Architecture of the Oman–UAE ophiolite: Evidence for a multi-phase magmatic history. *Arabian Journal of Geosciences*, 3, 439–458. <https://doi.org/10.1007/s12517-010-0177-3>
- Guilmette, C., Smit, M. A., van Hinsbergen, D. J. J., Gürer, D., Corfu, F., Charette, B., Maffione, M., Rabeau, O., & Savard, D. (2018). Forced subduction initiation recorded in the sole and crust of the Semail ophiolite of Oman. *Nature Geoscience*, 11, 688–695. <https://doi.org/10.1038/s41561-018-0209-2>
- Gurnis, M., Hall, C., & Lavier, L. (2004). Evolving force balance during incipient subduction. *Geochemistry, Geophysics, Geosystems*, 5. <https://doi.org/10.1029/2003GC000681>
- Haase, K. M., Freund, S., Koepke, J., Haufl, F., & Erdmann, M. (2015). Melts of sediments in the mantle wedge of the Oman ophiolite. *Geology*, 43, 275–278. <https://doi.org/10.1130/G36451.1>
- Hacker, B. R. (1990). Simulation of the metamorphic and deformational history of the metamorphic sole of the Oman ophiolite. *Journal of Geophysical Research*, 95, 4895–4907. <https://doi.org/10.1029/JB095iB04p04895>
- Hacker, B. R. (1991). The role of deformation in the formation of metamorphic gradients: Ridge subduction beneath the Oman ophiolite. *Tectonics*, 10, 455–473. <https://doi.org/10.1029/90TC02779>
- Hacker, B. R., & Gnos, E. (1997). The conundrum of Samail: Explaining the metamorphic history. *Tectonophysics*, 279, 215–226. [https://doi.org/10.1016/S0040-1951\(97\)00114-5](https://doi.org/10.1016/S0040-1951(97)00114-5)
- Hacker, B. R., & Mosenfelder, J. L. (1996). Metamorphism and deformation along the emplacement thrust of the Samail ophiolite, Oman. *Earth and Planetary Science Letters*, 144, 435–451. [https://doi.org/10.1016/S0012-821X\(96\)00186-0](https://doi.org/10.1016/S0012-821X(96)00186-0)
- Hacker, B. R., Mosenfelder, J. L., & Gnos, E. (1996). Rapid emplacement of the Oman ophiolite: Thermal and geochronologic constraints. *Tectonics*, 15, 1230–1247. <https://doi.org/10.1029/96TC01973>
- Hall, C. E., Gurnis, M., Sdrolias, M., Lavier, L. L., & Müller, R. D. (2003). Catastrophic initiation of subduction following forced convergence across fracture zones. *Earth and Planetary Science Letters*, 212, 15–30. [https://doi.org/10.1016/S0012-821X\(03\)00242-5](https://doi.org/10.1016/S0012-821X(03)00242-5)
- Harrison, T. M. (1982). Diffusion of <sup>40</sup>Ar in hornblende. *Contributions to Mineralogy and Petrology*, 78, 324–331.
- Hermann, J., & Rubatto, D. (2003). Relating zircon and monazite domains to garnet growth zones: Age and duration of granulite facies metamorphism in the Val Malenco lower crust. *Journal of Metamorphic Geology*, 21, 833–852. <https://doi.org/10.1046/j.1525-1314.2003.00484.x>
- Hokada, T., & Harley, S. L. (2004). Zircon growth in UHT leucosome: Constraints from zircon-garnet rare earth elements (REE) relations in Napier complex, East Antarctica. *Journal of Mineralogical and Petrological Sciences*, 99, 180–190. <https://doi.org/10.2465/jmps.99.180>

- Holder, R. M., Hacker, B. R., Seward, G. G. E., & Kylander-Clark, A. R. C. (2019). Interpreting titanite U–Pb dates and Zr thermobarometry in high-grade rocks: Empirical constraints on elemental diffusivities of Pb, Al, Fe, Zr, Nb, and Ce. *Contributions to Mineralogy and Petrology*, 174, 42. <https://doi.org/10.1007/s00410-019-1578-2>
- Holt, A. F., & Condit, C. B. (2021). Slab temperature evolution over the lifetime of a subduction zone. *Geochemistry, Geophysics, Geosystems*, 22, e2020GC009476.
- Hopson, C. A., Coleman, R. G., Gregory, R. T., Pallister, J. S., & Bailey, E. H. (1981). Geologic section through the Samail ophiolite and associated rocks along a Muscat-Ibra transect, south-eastern Oman Mountains. *Journal of Geophysical Research*, 86, 2527–2544. <https://doi.org/10.1029/JB086iB04p02527>
- Ishikawa, T., Fujisawa, S., Nagaishi, K., & Masuda, T. (2005). Trace element characteristics of the fluid liberated from amphibolite-facies slab: Inference from the metamorphic sole beneath the Oman ophiolite and implication for boninite genesis. *Earth and Planetary Science Letters*, 240, 355–377. <https://doi.org/10.1016/j.epsl.2005.09.049>
- Ishikawa, T., Nagaishi, K., & Umino, S. (2002). Boninitic volcanism in the Oman ophiolite: Implications for thermal condition during transition from spreading ridge to arc. *Geology*, 30, 899–902. [https://doi.org/10.1130/0091-7613\(2002\)030<0899:BVITOO>2.0.CO;2](https://doi.org/10.1130/0091-7613(2002)030<0899:BVITOO>2.0.CO;2)
- Kelemen, P. B., Carlos de Obeso, J., Leong, J. A., Godard, M., Okazaki, K., Kotowski, A. J., Manning, C. E., Ellison, E. T., Menzel, M. D., Urai, J. L., Hirth, G., Rioux, M., Stockli, D. F., Lafay, R., Beinlich, A. M., Coggon, J. A., Warsi, N. H., Matter, J. M., Teagle, D. A. H., ... The Oman Drilling Project Science Team. (2022). Listvenite formation during mass transfer into the leading edge of the mantle wedge: Initial results from Oman Drilling Project Hole BT1B. *Journal of Geophysical Research: Solid Earth*, 127, e2021JB022352. <https://doi.org/10.1029/2021JB022352>
- Kelemen, P. B., Koga, K., & Shimizu, N. (1997). Geochemistry of gabbro sills in the crust-mantle transition zone of the Oman ophiolite: Implications for the origin of the oceanic lower crust. *Earth and Planetary Science Letters*, 146, 475–488. [https://doi.org/10.1016/S0012-821X\(96\)00235-X](https://doi.org/10.1016/S0012-821X(96)00235-X)
- Kelly, N. M., & Harley, S. L. (2005). An integrated microtextural and chemical approach to zircon geochronology: Refining the Archaean history of the Napier complex, East Antarctica. *Contributions to Mineralogy and Petrology*, 149, 57–84. <https://doi.org/10.1007/s00410-004-0635-6>
- Kim, S., Jang, Y., Kwon, S., Samuel, V. O., Kim, S. W., Park, S.-I., Santosh, M., & Kokkalas, S. (2020). Petro-tectonic evolution of metamorphic sole of the Semail ophiolite, UAE. *Gondwana Research*, 86, 203–221. <https://doi.org/10.1016/j.gr.2020.05.013>
- Kohn, M. J., & Kelly, N. M. (2018). Petrology and geochronology of metamorphic zircon. In D. E. Moser, F. Corfu, J. R. Darling, S. M. Reddy, & K. Tait (Eds.), *Microstructural geochronology: Planetary records down to atom scale, geophysical monograph* 232 (1st ed.). John Wiley & Sons, Inc. <https://doi.org/10.1002/9781119227250.ch2>
- Kotowski, A. J., Cloos, M., Stockli, D. F., & Orent, E. B. (2021). Structural and thermal evolution of an infant subduction shear zone: Insights from sub-ophiolite metamorphic rocks recovered from Oman Drilling Project Site BT-1B. *Journal of Geophysical Research*, 126, e2021JB021702. <https://doi.org/10.1029/2021JB021702>
- Kovacs, N., Allan, M. M., Crowley, J. L., Colpron, M., Hart, C. J. R., Zagorevski, A., & Creaser, R. A. (2020). Carmacks copper Cu–Au–Ag deposit: Mineralization and Postore migmatization of a stikine arc porphyry copper system in Yukon, Canada. *Economic Geology*, 115, 1413–1442. <https://doi.org/10.5382/econgeo.4756>
- Kusano, Y., Adachi, Y., Miyashita, S., & Umino, S. (2012). Lava accretion system around mid-ocean ridges: Volcanic stratigraphy in the Wadi Fihz area, northern Oman ophiolite. *Geochemistry, Geophysics, Geosystems*, 13, Q05012.
- Kusano, Y., Hayashi, M., Adachi, Y., Umino, S., & Miyashita, S. (2014). Evolution of volcanism and magmatism during initial arc stage: Constraints on the tectonic setting of the Oman ophiolite. *Geological Society, London, Special Publications*, 392, 177–193. <https://doi.org/10.1144/SP392.9>
- Kusano, Y., Umino, S., Shinjo, R., Ikei, A., Adachi, Y., Miyashita, S., & Arai, S. (2017). Contribution of slab-derived fluid and sedimentary melt in the incipient arc magmas with development of the paleo-arc in the Oman ophiolite. *Chemical Geology*, 449, 206–225. <https://doi.org/10.1016/j.chemgeo.2016.12.012>
- Kylander-Clark, A. R. C., Hacker, B. R., & Cottle, J. M. (2013). Laser-ablation split-stream ICP petrochronology. *Chemical Geology*, 345, 99–112. <https://doi.org/10.1016/j.chemgeo.2013.02.019>
- Leng, W., Gurnis, M., & Asimow, P. (2012). From basalts to boninites: The geodynamics of volcanic expression during induced subduction initiation. *Lithosphere*, 4, 511–523. <https://doi.org/10.1130/L215.1>
- MacLeod, C. J., Lissenberg, C. J., & Bibby, L. E. (2013). “Moist MORB” axial magmatism in the Oman ophiolite: The evidence against a mid-ocean ridge origin. *Geology*, 41, 459–462. <https://doi.org/10.1130/G33904.1>
- MacLeod, C. J., & Rothery, D. A. (1992). Ridge axial segmentation in the Oman ophiolite: Evidence from along-strike variations in the sheeted dyke complex. *Geological Society, London, Special Publications*, 60, 39–63. <https://doi.org/10.1144/GSL.SP.1992.060.01.03>
- Mattinson, J. M. (2005). Zircon U/Pb chemical abrasion (CA-TIMS) method: Combined annealing and multi-step partial dissolution analysis for improved precision and accuracy of zircon ages. *Chemical Geology*, 220, 47–66. <https://doi.org/10.1016/j.chemgeo.2005.03.011>
- Maunder, B., Prytulak, J., Goes, S., & Reagan, M. (2020). Rapid subduction initiation and magmatism in the Western Pacific driven by internal vertical forces. *Nature Communications*, 11, 1874. <https://doi.org/10.1038/s41467-020-15737-4>
- McLean, N. M., Bowring, J. F., & Bowring, S. A. (2011). An algorithm for U–Pb isotope dilution data reduction and uncertainty propagation. *Geochemistry, Geophysics, Geosystems*, 12. <https://doi.org/10.1029/2010GC003478>
- Montigny, R., le Mer, O., Thuizat, R., & Whitechurch, H. (1988). K–Ar and Ar study of metamorphic rocks associated with the Oman ophiolite: Tectonic implications. *Tectonophysics*, 151, 345–362. [https://doi.org/10.1016/0040-1951\(88\)90252-1](https://doi.org/10.1016/0040-1951(88)90252-1)
- Morris, A., Meyer, M., Anderson, M. W., & MacLeod, C. J. (2016). Clockwise rotation of the entire Oman ophiolite occurred in a



- suprasubduction zone setting. *Geology*, 44, 1055–1058. <https://doi.org/10.1130/G38380.1>
- Nicolas, A. (1989). *Structures of ophiolites and dynamics of oceanic lithosphere*. Springer. <https://doi.org/10.1007/978-94-009-2374-4>
- Nicolas, A., & Boudier, F. (2017). Emplacement of Semail-emirates ophiolite at ridge-trench collision. *Terra Nova*, 29, 127–134. <https://doi.org/10.1111/ter.12256>
- Nicolas, A., Boudier, F., & Ildefonse, B. (1996). Variable crustal thickness in the Oman ophiolite: Implication for oceanic crust. *Journal of Geophysical Research*, 101, 17941–17950. <https://doi.org/10.1029/96JB00195>
- Nicolas, A., Boudier, F., Ildefonse, B., & Ball, E. (2000). Accretion of Oman and United Arab Emirates ophiolite—Discussion of a new structural map. *Marine Geophysical Research*, 21, 147–180.
- Nicolas, A., Reuber, I., & Benn, K. (1988). A new magma chamber model based on structural studies in the Oman ophiolite. *Tectonophysics*, 151, 87–105. [https://doi.org/10.1016/0040-1951\(88\)90242-9](https://doi.org/10.1016/0040-1951(88)90242-9)
- Nikolaeva, K., Gerya, T. V., & Connolly, J. A. D. (2008). Numerical modelling of crustal growth in intraoceanic volcanic arcs. *Physics of the Earth and Planetary Interiors*, 171, 336–356. <https://doi.org/10.1016/j.pepi.2008.06.026>
- Pallister, J. S., & Hopson, C. A. (1981). Samail ophiolite plutonic suite: Field relations, phase variation, cryptic variation and layering, and a model of a spreading ridge magma chamber. *Journal of Geophysical Research*, 86, 2593–2644. <https://doi.org/10.1029/JB086iB04p02593>
- Peacock, S. M. (1991). Numerical simulation of subduction zone pressure-temperature-time paths: Constraints on fluid production and arc magmatism. *Philosophical transactions of the Royal Society of London. Series a: Physical and Engineering Sciences*, 335, 341–353.
- Peacock, S. M. (1996). Thermal and petrologic structure of subduction zones. *Subduction: Top to Bottom*, 96, 119–133.
- Pearce, J. A., Alabaster, T., Shelton, A. W., & Searle, M. P. (1981). The Oman ophiolite as a cretaceous arc-basin complex: Evidence and implications. *Philosophical transactions of the Royal Society of London. Series a, Mathematical and Physical Sciences*, 300, 299–317.
- Phipps Morgan, J., & Chen, Y. J. (1993). The genesis of oceanic crust: Magma injection, hydrothermal circulation, and crustal flow. *Journal of Geophysical Research: Solid Earth*, 98, 6283–6297. <https://doi.org/10.1029/92JB02650>
- Prigent, C., Agard, P., Guillot, S., Godard, M., & Dubacq, B. (2018). Mantle wedge (De)formation during subduction infancy: Evidence from the base of the Semail Ophiolitic mantle. *Journal of Petrology*, 59, 2061–2092. <https://doi.org/10.1093/petrology/egy090>
- Prigent, C., Guillot, S., Agard, P., & Ildefonse, B. (2018). Fluid-assisted deformation and strain localization in the cooling mantle wedge of a young subduction zone (Semail ophiolite). *Journal of Geophysical Research: Solid Earth*, 123, 7529–7549. <https://doi.org/10.1029/2018JB015492>
- Prigent, C., Guillot, S., Agard, P., Lemarchand, D., Soret, M., & Ulrich, M. (2018). Transfer of subduction fluids into the deforming mantle wedge during nascent subduction: Evidence from trace elements and boron isotopes (Semail ophiolite, Oman). *Earth and Planetary Science Letters*, 484, 213–228. <https://doi.org/10.1016/j.epsl.2017.12.008>
- Quick, J. E., & Denlinger, R. P. (1993). Ductile deformation and the origin of layered gabbro in ophiolites. *Journal of Geophysical Research*, 98, 14015–14027.
- Reagan, M. K., Heaton, D. E., Schmitz, M. D., Pearce, J. A., Shervais, J. W., & Koppers, A. A. P. (2019). Forearc ages reveal extensive short-lived and rapid seafloor spreading following subduction initiation. *Earth and Planetary Science Letters*, 506, 520–529. <https://doi.org/10.1016/j.epsl.2018.11.020>
- Reagan, M. K., Ishizuka, O., Stern, R. J., Kelley, K. A., Ohara, Y., Blichert-Toft, J., Bloomer, S. H., Cash, J., Fryer, P., Hanan, B. B., Hickey-Vargas, R., Ishii, T., Kimura, J.-I., Peate, D. W., Rowe, M. C., & Woods, M. (2010). Fore-arc basalts and subduction initiation in the Izu-Bonin-Mariana system. *Geochemistry, Geophysics, Geosystems*, 11, Q03X12. <https://doi.org/10.1029/2009GC002871>
- Reagan, M. K., Pearce, J. A., Petronotis, K., Almeev, R. R., Avery, A. J., Carvallo, C., Chapman, T., Christeson, G. L., Ferré, E. C., Godard, M., Heaton, D. E., Kirchenbaur, M., Kurz, W., Kutterolf, S., Li, H., Li, Y., Michibayashi, K., Morgan, S., Nelson, W. R., ... Whattam, S. A. (2017). Subduction initiation and ophiolite crust: New insights from IODP drilling. *International Geology Review*, 59, 1439–1450. <https://doi.org/10.1080/00206814.2016.1276482>
- Rioux, M., Benoit, M., Amri, I., Ceuleneer, G., Garber, J. M., Searle, M., & Leal, K. (2021). The origin of felsic intrusions within the mantle section of the Samail ophiolite: Geochemical evidence for three distinct mixing and fractionation trends. *Journal of Geophysical Research: Solid Earth*, 126, e2020JB020760. <https://doi.org/10.1029/2020JB020760>
- Rioux, M., Bowring, S., Cheadle, M., & John, B. (2015). Evidence for initial excess  $^{231}\text{Pa}$  in mid-ocean ridge zircons. *Chemical Geology*, 397, 143–156. <https://doi.org/10.1016/j.chemgeo.2015.01.011>
- Rioux, M., Bowring, S. A., Kelemen, P. B., Gordon, S., Dudás, F., & Miller, R. (2012). Rapid crustal accretion and magma assimilation in the Oman-U.A.E. ophiolite: High precision U-Pb zircon geochronology of the gabbroic crust. *Journal of Geophysical Research*, 117. <https://doi.org/10.1029/2012JB009273>
- Rioux, M., Bowring, S., Kelemen, P., Gordon, S., Miller, R., & Dudás, F. (2013). Tectonic development of the Samail ophiolite: High-precision U-Pb zircon geochronology and Sm-Nd isotopic constraints on crustal growth and emplacement. *Journal of Geophysical Research*, 118, 2085–2101. <https://doi.org/10.1002/jgrb.50139>
- Rioux, M., Garber, J., Bauer, A., Bowring, S., Searle, M., Kelemen, P., & Hacker, B. (2016). Synchronous formation of the metamorphic sole and igneous crust of the Semail ophiolite: New constraints on the tectonic evolution during ophiolite formation from high-precision U-Pb zircon geochronology. *Earth and Planetary Science Letters*, 451, 185–195.
- Rioux, M., Garber, J. M., Searle, M., Kelemen, P., Miyashita, S., Adachi, Y., & Bowring, S. (2021). High-precision U-Pb zircon dating of late magmatism in the Samail ophiolite: A record of subduction initiation. *Journal of Geophysical Research: Solid Earth*, 126, e2020JB020758.
- Rollinson, H. (2014). Plagiogranites from the mantle section of the Oman ophiolite: Models for early crustal evolution. *Geological Society, London, Special Publications*, 392, 247–261. <https://doi.org/10.1144/SP392.13>



- Rollinson, H. (2015). Slab and sediment melting during subduction initiation: Granitoid dykes from the mantle section of the Oman ophiolite. *Contributions to Mineralogy and Petrology*, 170, 1–20.
- Rubatto, D. (2002). Zircon trace element geochemistry: Partitioning with garnet and the link between U–Pb ages and metamorphism. *Chemical Geology*, 184, 123–138. [https://doi.org/10.1016/S0009-2541\(01\)00355-2](https://doi.org/10.1016/S0009-2541(01)00355-2)
- Rubatto, D., & Hermann, J. (2003). Zircon formation during fluid circulation in eclogites (Monviso, Western Alps): Implications for Zr and Hf budget in subduction zones. *Geochimica et Cosmochimica Acta*, 67, 2173–2187. [https://doi.org/10.1016/S0016-7037\(02\)01321-2](https://doi.org/10.1016/S0016-7037(02)01321-2)
- Rubatto, D., & Hermann, J. (2007). Experimental zircon/melt and zircon/garnet trace element partitioning and implications for the geochronology of crustal rocks. *Chemical Geology*, 241, 38–61. <https://doi.org/10.1016/j.chemgeo.2007.01.027>
- Scherer, E. E., Cameron, K. L., & Blichert-Toft, J. (2000). Lu–Hf garnet geochronology: Closure temperature relative to the Sm–Nd system and the effects of trace mineral inclusions. *Geochimica et Cosmochimica Acta*, 64, 3413–3432. [https://doi.org/10.1016/S0016-7037\(00\)00440-3](https://doi.org/10.1016/S0016-7037(00)00440-3)
- Searle, M., & Cox, J. (1999). Tectonic setting, origin, and obduction of the Oman ophiolite. *Geological Society of America Bulletin*, 111, 104–122. [https://doi.org/10.1130/0016-7606\(1999\)111<0104:TSOAOO>2.3.CO;2](https://doi.org/10.1130/0016-7606(1999)111<0104:TSOAOO>2.3.CO;2)
- Searle, M., & Cox, J. (2002). Subduction zone metamorphism during formation and emplacement of the Semail ophiolite in the Oman Mountains. *Geological Magazine*, 139, 241–255.
- Searle, M. P. (1985). Sequence of thrusting and origin of culminations in the northern and Central Oman Mountains. *Journal of Structural Geology*, 7, 129–143.
- Searle, M. P., Lippard, S. J., Smewing, J. D., & Rex, D. C. (1980). Volcanic rocks beneath the Semail ophiolite nappe in the northern Oman mountains and their significance in the Mesozoic evolution of Tethys. *Journal of the Geological Society, London*, 137, 589–604. <https://doi.org/10.1144/gsjgs.137.5.0589>
- Searle, M. P., & Malpas, J. (1980). The structure and metamorphism of rocks beneath the Semail ophiolite of Oman and their significance in ophiolite obduction. *Transactions of the Royal Society of Edinburgh, Earth Sciences*, 71, 247–262. <https://doi.org/10.1017/S0263593300013614>
- Searle, M. P., & Malpas, J. (1982). Petrochemistry and origin of sub-ophiolitic metamorphic and related rocks in the Oman Mountains. *Journal of the Geological Society, London*, 139, 235–248. <https://doi.org/10.1144/gsjgs.139.3.0235>
- Searle, M. P., Rioux, M., & Garber, J. M. (2022). One line on the map: A review of the geological history of the Semail Thrust, Oman-UAE Mountains. *Journal of Structural Geology*, 158, 104594. <https://doi.org/10.1016/j.jsg.2022.104594>
- Searle, M. P., Waters, D. J., Garber, J. M., Rioux, M., Cherry, A. G., & Ambrose, T. K. (2015). Structure and metamorphism beneath the obducting Oman ophiolite: Evidence from the Bani Hamid granulites, northern Oman mountains. *Geosphere*, 11, 1812–1836. <https://doi.org/10.1130/GES01199.1>
- Soret, M., Agard, P., Dubacq, B., Plunder, A., & Yamato, P. (2017). Petrological evidence for stepwise accretion of metamorphic soles during subduction infancy (Semail ophiolite, Oman and UAE). *Journal of Metamorphic Geology*, 35, 1051–1080. <https://doi.org/10.1111/jmg.12267>
- Soret, M., Agard, P., Ildefonse, B., Dubacq, B., Prigent, C., & Rosenberg, C. (2019). Deformation mechanisms in mafic amphibolites and granulites: Record from the Semail metamorphic sole during subduction infancy. *Solid Earth*, 10, 1733–1755. <https://doi.org/10.5194/se-10-1733-2019>
- Soret, M., Bonnet, G., Agard, P., Larson, K. P., Cottle, J. M., Dubacq, B., Kylander-Clark, A. R. C., Button, M., & Rividi, N. (2022). Timescales of subduction initiation and evolution of subduction thermal regimes. *Earth and Planetary Science Letters*, 584, 117521. <https://doi.org/10.1016/j.epsl.2022.117521>
- Spencer, C. J., Cavosie, A. J., Raub, T. D., Rollinson, H., Jeon, H., Searle, M. P., Miller, J. A., McDonald, B. J., Evans, N. J., & Edinburgh Ion Microprobe, F. (2017). Evidence for melting mud in Earth's mantle from extreme oxygen isotope signatures in zircon. *Geology*, 45, 975–978. <https://doi.org/10.1130/G39402.1>
- Stacey, J. S., & Kramers, J. D. (1975). Approximation of terrestrial lead isotope evolution by a two-stage model. *Earth and Planetary Science Letters*, 26, 207–221. [https://doi.org/10.1016/0012-821X\(75\)90088-6](https://doi.org/10.1016/0012-821X(75)90088-6)
- Stern, R. J. (2004). Subduction initiation: Spontaneous and induced. *Earth and Planetary Science Letters*, 226, 275–292. [https://doi.org/10.1016/S0012-821X\(04\)00498-4](https://doi.org/10.1016/S0012-821X(04)00498-4)
- Stern, R. J., & Bloomer, S. H. (1992). Subduction zone infancy: Examples from the Eocene Izu-Bonin-Mariana and Jurassic California arcs. *Geological Society of America Bulletin*, 104, 1621–1636. [https://doi.org/10.1130/0016-7606\(1992\)104<1621:SZIEFT>2.3.CO;2](https://doi.org/10.1130/0016-7606(1992)104<1621:SZIEFT>2.3.CO;2)
- Stern, R. J., & Gerya, T. (2018). Subduction initiation in nature and models: A review. *Tectonophysics*, 746, 173–198. <https://doi.org/10.1016/j.tecto.2017.10.014>
- Stern, R. J., Reagan, M., Ishizuka, O., Ohara, Y., & Whattam, S. (2012). To understand subduction initiation, study forearc crust: To understand forearc crust, study ophiolites. *Lithosphere*, 4, 469–483. <https://doi.org/10.1130/L183.1>
- Styles, M. T., Ellison, R. A., Phillips, E. R., Arkley, S., Schofield, D. I., Thomas, R. J., Goodenough, K. M., Farrant, A. R., McKerver, J. A., Crowley, Q. G., & Pharaoh, T. C. (2006). *The geology and geophysics of the United Arab Emirates* (Vol. 2). Ministry of Energy, United Arab Emirates.
- Syracuse, E. M., van Keken, P. E., & Abers, G. A. (2010). The global range of subduction zone thermal models. *Physics of the Earth and Planetary Interiors*, 183, 73–90. <https://doi.org/10.1016/j.pepi.2010.02.004>
- Taylor, R. J. M., Clark, C., Harley, S. L., Kylander-Clark, A. R. C., Hacker, B. R., & Kinny, P. D. (2017). Interpreting granulite facies events through rare earth element partitioning arrays. *Journal of Metamorphic Geology*, 35, 759–775. <https://doi.org/10.1111/jmg.12254>
- Taylor, R. J. M., Harley, S. L., Hinton, R. W., Elphick, S., Clark, C., & Kelly, N. M. (2015). Experimental determination of REE partition coefficients between zircon, garnet and melt: A key to understanding high-T crustal processes. *Journal of Metamorphic Geology*, 33, 231–248. <https://doi.org/10.1111/jmg.12118>
- Tilton, G. R., Hopson, C. A., & Wright, J. E. (1981). Uranium-lead isotopic ages of the Samail ophiolite, Oman, with applications to Tethyan ocean ridge tectonics. *Journal of Geophysical Research*, 86, 2763–2775. <https://doi.org/10.1029/JB086iB04p02763>

- van Hinsbergen, D. J. J., Maffione, M., Koornneef, L. M. T., & Guilmette, C. (2019). Kinematic and paleomagnetic restoration of the Semail ophiolite (Oman) reveals subduction initiation along an ancient Neotethyan fracture zone. *Earth and Planetary Science Letters*, 518, 183–196. <https://doi.org/10.1016/j.epsl.2019.04.038>
- Vermeesch, P. (2018). IsoplotR: A free and open toolbox for geochronology. *Geoscience Frontiers*, 9, 1479–1493.
- Warren, C., Parrish, R., Waters, D., & Searle, M. (2005). Dating the geologic history of Oman's Semail ophiolite: Insights from U-Pb geochronology. *Contributions to Mineralogy and Petrology*, 150, 403–422. <https://doi.org/10.1007/s00410-005-0028-5>
- Wendt, I., & Carl, C. (1991). The statistical distribution of the mean squared weighted deviation. *Chemical Geology*, 86, 275–285.
- Whitehouse, M. J., & Platt, J. P. (2003). Dating high-grade metamorphism—Constraints from rare-earth elements in zircon and garnet. *Contributions to Mineralogy and Petrology*, 145, 61–74. <https://doi.org/10.1007/s00410-002-0432-z>
- Zhou, X., & Wada, I. (2021). Differentiating induced versus spontaneous subduction initiation using thermomechanical models and metamorphic soles. *Nature Communications*, 12, 4632. <https://doi.org/10.1038/s41467-021-24896-x>

## SUPPORTING INFORMATION

Additional supporting information can be found online in the Supporting Information section at the end of this article.

**Figure S1.** Cathodoluminescence (CL) images of analyzed zircon, including laser ablation spot locations. Spot numbers correspond to blue (Yb/Dy > 5), red (Yb/Dy < 5), and gray (imprecise Yb/Dy) trace element spots. Spot locations and sizes are approximate.

**Figure S2.** Laser milling of grain TA-16 iz1. (a–c) CL images of each side of the polished grain, with spot locations. Numbers next to spots are measured Yb/Dy. Dashed white lines outline where the laser cuts were made. Blue spots have Yb/Dy > 5, red spots have Yb/Dy < 5, and black spots have Yb/Dy with high uncertainties. Spot analyses from panel (a) were analyzed at Boise State University and the data are not reported in this manuscript. (d) Reflected light image of the cut grain. Small holes in (c) and (d) are a grid of laser pits used to guide the cutting. (e) Transmitted light images of the plucked grain fragments.

**Figure S3.** Laser milling of grain TA-16 iz14. (a–b) CL images of each side of the polished grain, with spot locations. Numbers next to spots are measured Yb/Dy. Dashed white lines outline where the laser cut was made. Blue spots have Yb/Dy > 5, red spots have Yb/Dy < 5, and black spots have Yb/Dy with high uncertainties. Spot analyses from panel (b) were analyzed at Boise State University and the data are not reported in this manuscript. (c) SEM image of the cut grain.

**Figure S4.** Cathodoluminescence images of micro-sampled grains. Grains were broken into multiple pieces along yellow dashed lines. In all panels, blue spots have Yb/Dy > 5, red spots have Yb/Dy < 5, black spots have Yb/Dy with high uncertainties, and white fragment numbers (e.g., iz40-1) correspond to fragment dates in Table S2 and Figures 5. Numbers within the spots are the spot numbers (Table S1), and red and blue numbers beside spots are the measured Yb/Dy. All other micro-sampled grains are shown in Figures 2, S2, and S3.

**Figure S5.** Additional zircon trace element data for the garnet-clinopyroxene amphibolites, garnet-free amphibolites, and leucocratic pods dated in this study. Gray data on the plots of Dy versus unnormalized Yb/Dy show the range of data in garnet-free amphibolites and leucocratic pods from this study. A limited number of data points were excluded or plot off scale, as outlined in the Supplemental Text.

**Figure S6.** P-T pseudosections calculated for an average garnet-clinopyroxene bearing amphibolite composition (a) and an average garnet-clinopyroxene-free amphibolite composition (b) using the Gibbs free-energy minimization software *Perple\_X* (Connolly, 2005), version 6.8.4. The bulk compositions for analysis were sourced from Wadi Tayin amphibolite bulk compositions measured by Ishikawa et al. (2005), with compositional averages calculated as geometric means of the data ( $n=7$  for the garnet amphibolites and  $n=5$  for the garnet-free amphibolites). For all calculations, we used the Holland and Powell (2011) thermodynamic dataset, with  $H_2O$  modeled using the CORK model of Holland and Powell (1991), and sufficient  $H_2O$  to saturate each bulk composition at its respective solidus. Thermodynamic modelling was performed in the system  $SiO_2$ - $TiO_2$ - $Al_2O_3$ - $FeO$ - $Fe_2O_3$ - $MnO$ - $MgO$ - $CaO$ - $Na_2O$ - $K_2O$ - $H_2O$ .  $Fe^{3+}$  was cast as 20% of total Fe. Solution models for the calculation were as follows: Gt (W) for garnet, Bi(W) for biotite, Mica(W) for white mica, Crd(W) for cordierite, Chl(W) for chlorite, Ilm(WPH) for ilmenite, and Opx(W) for orthopyroxene (White et al., 2014a; White et al., 2014b); Augite(G) for clinopyroxene, cAmph(G) for clinoamphibole, and melt(G) for tonalitic melt (Green et al., 2016); Ep(HP11) for epidote (Holland and Powell, 2011); Sp(WPC) for spinel (White et al., 2002); feldspar for plagioclase (Fuhrman and Lindsley, 1988); and T for ideal talc. Silica and titania activities were calculated after Ashley and Law (2015) by ratioing the chemical potentials calculated for  $SiO_2$  and  $TiO_2$  to those determined for quartz and rutile (respectively) over the entire P-T grid. Ti-bearing phase boundaries are also shown for each bulk composition; the Ti-phase relations in “HTa” amphibolites are most consistent with those observed in the clinopyroxene- and garnet-bearing amphibolite bulk composition.

**Figure S7.** The difference between average Ti-in-zircon temperatures for spots with Yb/Dy > 5 and Yb/Dy < 5 versus the maximum observed Ti-in-zircon temperature (a) and the average Ti-in-zircon temperature for zircon with Yb/Dy < 5 (b) for each sample.

**Figure S8.** Comparison of zircon-garnet partition coefficients from this study and existing experiments. Blue crosses are garnet-zircon partition coefficients calculated for zircon with Yb/Dy > 5 and an average high Yb/Dy garnet composition from the sample (core). Red crosses are garnet-zircon partition coefficients calculated for zircon with Yb/Dy < 5 and an average low Yb/Dy garnet composition (rim). Gray squares and circles show the experimental data of Rubatto and Hermann (2007) and Taylor et al. (2015), respectively. The center column shows garnet Yb/Dy concentrations versus unitless distance along the analyzed transect. The dashed blue box is the data used to calculate an average high (core) garnet Yb/Dy and the red box is the data used to calculate an average low (rim) garnet Yb/Dy value. For sample 171219J03/171219M06 we used an average value of all the garnet Yb/Dy data to calculate the zircon-garnet partition coefficients. The right column shows garnet Ca and Mg concentrations (wt.%) along the same transect as the Yb/Dy data.

**Figure S9.** Backscattered electron images of zircon inclusions within garnet in garnet amphibolites from

metamorphic sole localities. (a-c) Thin sections of samples from Hammah (a; 171213J02), Fanjah (b; 171214J01), and Sumeini (c; 171219J03). (d-h) Zircon inclusions within garnet in grain mounts from samples from Masafi (d; 181221M04) and Hammah (e-h; sample 171213J02). Samples 171213J02 and 181221M04 were dated in this study. Each zircon inclusion was verified by energy dispersive spectroscopy.

**Table S1.** Laser ablation-inductively coupled plasma-mass spectrometry (LA-ICP-MS) zircon U-Pb and trace element data.

**Table S2.** ID-TIMS U-Pb zircon data.

**Table S3.** Zircon Lu-Hf isotopic data.

**Table S4.** LA-ICP-MS analyses of garnet, amphibole, clinopyroxene, and titanite.

#### Supplemental Text

**How to cite this article:** Rioux, M., Garber, J. M., Searle, M., Crowley, J. L., Stevens, S., Schmitz, M., Kylander-Clark, A., Leal, K., Ambrose, T., & Smye, A. J. (2023). The temporal evolution of subduction initiation in the Samail ophiolite: High-precision U-Pb zircon petrochronology of the metamorphic sole. *Journal of Metamorphic Geology*, 41(6), 817–847. <https://doi.org/10.1111/jmg.12719>